JGR Solid Earth

RESEARCH ARTICLE
10.1029/2020JB021540

Key Points:
- Epidosite alteration strips Na + Mg from precursor spilite rocks, adds Ca and minor Al + Fe, and conserves Si and Ti
- Alteration to end-member epidosite entails water/rock ratios of 700–44,000 kg/kg
- Epidosite fluid chemistry is incompatible with black-smoker type vent fluids and cannot form seafloor sulfide deposits

Reaction Mechanism and Water/Rock Ratios Involved in Epidosite Alteration of the Oceanic Crust

Samuel Weber[1] [ID], **Larryn W. Diamond[1]** [ID], **Peter Alt-Epping[1]** [ID], and **Alannah C. Brett-Adams[1]**

[1]Institute of Geological Sciences, University of Bern, Bern, Switzerland

Abstract Epidosites are a prominent type of subseafloor hydrothermal alteration of basalts in ophiolites and greenstone belts, showing an end-member mineral assemblage of epidote + quartz + titanite + Fe-oxide. Epidosites are known to form within crustal-scale upflow zones and their fluids have been proposed as deep equivalents of black-smoker seafloor vent fluids. Proposals of the mass of fluid per mass of rock (W/R ratio) needed to form epidosites are contradictory, varying from 20 (Sr isotopes) to > 1,000 (Mg mobility). To test these proposals we have conducted a petrographic, geochemical and reactive-transport numerical simulation study of the chemical reaction that generates km^3-size epidosite zones within the lavas and sheeted dike complex of the Samail ophiolite, Oman. At 250–400°C the modeled epidosite-forming fluid has near-neutral pH (~ 5.2), high fO_2, low sulfur and very low Fe (10^{-6} mol/kg) contents. These features argue against a genetic link with black-smoker fluids. Chemical buffering by the epidosite fluid enriches the precursor spilites in Ca and depletes them in Na and Mg. Completion of the spilite-to-epidosite reaction requires enormous W/R ratios of 700–$\sim$40,000, depending on initial Mg content and temperature. Collectively, the variably altered rocks in the Samail epidosite zones record flow of $\sim 10^{15}$ kg of fluid through each km^3 of precursor spilite rock. This fluid imposed on the epidosite an Sr-isotope signature inherited from the previous rock-buffered chemical evolution of the fluid through the oceanic crust, thereby explaining the apparently contradictory low W/R ratios based on Sr isotopes.

1. Introduction

Basaltic oceanic crust typically exhibits extensive hydrothermal alteration (e.g., Staudigel, 2003). Geochemical and geophysical observations from seafloor drill holes, active hydrothermal vents, ophiolites, and experimental studies have led to a detailed understanding of how this alteration occurs (summarized by e.g., Alt, 1995; Berndt et al., 1989; Humphris & Klein, 2018; Seyfried et al., 1988; Staudigel, 2003). Buoyant rise of heated pore water above shallow intrusions draws distal cold seawater into the newly formed crust, generating convection cells. As the infiltrating seawater is heated along the *downflow* path, its dissolved Mg and sulfate are quantitatively stripped by fixation into hydrothermal clays, chlorite and anhydrite. The seawater also loses some of its Na due to albitization of plagioclase, gaining Ca instead (e.g., Mottl, 1983). These mineral reactions also affect trace element concentrations in the fluid, including Sr, which can be released during the alteration of igneous plagioclase or sequestered by precipitation of minerals (e.g., anhydrite). At temperatures of $\sim$250–450°C, these processes pervasively alter the basalts to an assemblage of albite + chlorite + Fe-oxides + titanite ± actinolite ± epidote. Such altered rocks can be referred to as *spilite* (in the sense of Cann, 1969; dikes altered to this assemblage in Troodos are also termed *diabase*, e.g., Richardson et al., 1987). Following this alteration, the chemically modified seawater, now depleted in Mg and enriched in Ca, cycles back to the seafloor as testified by the chemistry of hydrothermal vent fluids (e.g., Seyfried et al., 1988).

A second type of pervasive rock alteration known as *epidosite* has been recognized in ophiolites (e.g., Gillis & Banerjee, 2000; Harper et al., 1988; Juteau et al., 2000; Nehlig et al., 1994; Richardson et al., 1987; Schiffman & Smith, 1988) and in Archean greenstone belts (e.g., Galley, 1993; Hannington et al., 2002; Polat et al., 2007; White et al., 2014) but so far only rarely in present-day oceanic crust (Banerjee et al., 2000; Quon & Ehlers, 1963). Most mapped epidosite zones contain rocks variably enriched in epidote and quartz with only a fraction displaying the granoblastic end-member mineral assemblage of epidote + quartz + titanite ± Fe-oxides (e.g., Gilgen et al., 2016; Jowitt et al., 2012). Epidosite zones in the Troodos ophiolite occur as km^3 sized bodies at the base of the sheeted dike complex (SDC; Richardson et al., 1987). The mineralogy

of epidosites shows that they formed from a fluid enriched in Ca and depleted in Na and Mg, qualitatively similar to seafloor vent fluids (Richardson et al., 1987). Based on these features, epidosite zones have been proposed to form at the base of the *upflow* paths of hydrothermal convection cells (Richardson et al., 1987; Schiffman & Smith, 1988). Moreover, the fluids that form the epidosites have been viewed as deep equivalents of the black-smoker type seafloor vent fluids that generate massive sulfide deposits (Jowitt et al., 2012; Richardson et al., 1987; Schiffman & Smith, 1988). In the Samail ophiolite, epidosite zones are also present in the SDC but they are more abundant and larger (km^3 size) in the overlying lavas (Gilgen et al., 2016). The timing of epidosite alteration relative to crustal growth seems to be variable. Paleomagnetic evidence indicates that the Troodos epidosites formed during the axial-spreading stage of crust formation (Varga et al., 1999). In Samail, by contrast, cross-cutting relations of altered dikes and volcanic units show that the epidosites mostly formed after axial spreading had ceased. Thus, post-axial lavas as well as the underlying axial lavas and SDC are epidotized (Gilgen et al., 2016). For Troodos it has been proposed from crosscutting relationships that epidosite alteration directly overprinted fresh basalt in a dike-by-dike process during growth of the SDC (Cann et al., 2014, p. 9), but Gilgen et al. (2016) provided an alternative interpretation in which epidosite alteration occurs after local emplacement of the SDC. The field and petrographic relationships of the Samail epidosites show that they overprinted precursor spilites, indicating that they formed relatively late in the hydrothermal history over a range of subseafloor depths from a few hundred meters to as much as 3.5 km (Gilgen et al., 2016).

The fluid that causes epidosite alteration (hereafter referred to as the "epidosite fluid") is known to have salinity close to that of seawater (Nehlig et al., 1994; Richardson et al., 1987; Richter & Diamond, 2019; Schiffman & Smith, 1988) but it is not yet clear how deeply circulating seawater acquires high enough Ca and low enough Mg and Na contents to stabilize the end-member epidosite mineral assemblage (Seyfried et al., 1988). As a step toward understanding the significance of this alteration for oceanic hydrothermal systems, it is useful to characterize the chemistry of the epidosite fluid and to estimate how much of it is required to explain the huge volumes of epidotized rock in the ophiolite and greenstone terranes. This amount would reflect the late-stage integrated fluid flux through the upflow zones of hydrothermal circulation cells (e.g., Bickle & Teagle, 1992). Such zones are known to be important in transferring heat and mass from the crust to the oceans, and in channeling the metal-bearing fluids that feed massive sulfide ore deposits at the seafloor.

A striking chemical feature of end-member epidosites is their quantitative loss of Mg. As the solubility of Mg-bearing minerals deep in the crust is exceedingly low, it has been recognized that large amounts of water are required to leach all the Mg from the precursor rock during epidosite formation (e.g., Seyfried et al., 1988). Previous studies have estimated the cumulative mass of fluid that must pass through a fixed mass of rock, the water/rock ratio (*W/R*), to explain the formation of epidosite. Estimates vary from 20 to 1,250, thus the amount of fluid required is still highly uncertain.

This study first presents new mineralogical, petrographic and whole-rock chemical analyses from the Samail ophiolite, Oman, to elucidate the chemical mechanism of the spilite-to-epidosite reaction at the dm-m scale. The chemical composition of the epidosite fluid is reconstructed from thermodynamic and fluid inclusion constraints and compared to black-smoker type vent fluids. Knowledge of the fluid chemistry allows the new observations to be reproduced in numerical reactive-transport simulations that take account of mineral solubilities. These simulations reveal the key role of Mg-bearing minerals in controlling the *W/R* ratios involved in epidosite transformation, and they demonstrate the dependency of the ratio on different compositions of precursor spilites and temperatures of alteration. Finally, consideration of the different meanings of *W/R* ratios based on mineral solubility versus on Sr-isotopes leads to resolution of the apparently contradictory *W/R* estimates in the literature.

2. Geological Setting and Outcrop Features of the Samail Epidosite Zones

The Samail ophiolite in north-eastern Oman is part of a chain of Mid-Cretaceous Tethyan ophiolites (Lippard et al., 1986). It consists of a slice of upper lithosphere from a fast-spreading oceanic ridge, originally situated in a fore-arc setting above a nascent subduction zone (e.g., Belgrano & Diamond, 2019 and references

therein). The base of the upper crust is composed of a well-developed 1–1.5 km thick SDC, overlain by a 1–3 km thick extrusive sequence. The basal lava unit (Geotimes) is comagmatic with the SDC and consists of spreading-axis basalts and basaltic andesites. This unit transitions upwards into off-axis primitive basalts (Lasail) and a post-spreading sequence of basalt, basaltic andesite and boninite lavas (Tholeiitic Alley and Boninitic Alley units), all capped by pelagic sediments (Belgrano et al., 2019; Lippard et al., 1986). The presence of post-axial lavas up to 2 km thick is a major difference between the Samail ophiolite and much of the in situ MOR-type crust underlying today's oceans. After its emplacement onto the Arabian continent, the ophiolite was folded into a regional-scale northwest-southeast striking anticline. In the eastern limb of the anticline, today's erosional surface exposes a several hundred kilometer long oblique cut through the SDC and the extrusive rocks.

The dozens of known epidosite zones in the Samail lavas occur as well-defined tabular or equidimensional bodies, some with surface exposures of more than a square kilometer (Gilgen et al., 2016). They most commonly overprint the more permeable pillow lavas, but also massive lava flows and dikes are altered. In outcrops, the epidosites are easily distinguished from the surrounding spilites by their distinctive pistachio-green color and their massive, granoblastic texture. As shown by detailed mapping, the epidosite alteration pervasively affects large volumes of the sparsely fractured host-rock, indicating that it formed principally via broad porous-medium flow rather than flow focused through fracture networks (Gilgen et al., 2016). Epidotization of spilitized pillow stacks follows a concentric, mappable pattern at the 10–100 m scale, reflecting the relative permeability of the constituent lava components. In the distal region only the interpillow hyaloclastite is altered to end-member epidosite. This passes inwards to a region where the cores of pillows show nodular patches of epidosite surrounded by relict spilite (Figure 1a), progressing to pillow cores that are macroscopically completely altered epidosite. In the centers of the major epidosite bodies, pillow rims as well as interpillow hyaloclastites and pillow cores are completely altered to epidosite (Gilgen et al., 2016). Massive lava flows commonly show nodular epidosite alteration, whereas feeder dikes in the lavas and sheeted dikes in the SDC typically show striped alternation of spilite and epidosite parallel to the dikes (Gilgen et al., 2016; this striping is also typical of the Troodos dikes, e.g., Cann et al., 2014; Jowitt et al., 2012). The transition from spilite to epidosite along the margins of individual epidosite nodules and stripes in dikes is sharp (5–15 cm wide; Figure 1a), attesting to strong channeling of hydrothermal fluid and permitting sampling of the entire spilite-to-epidosite reaction front in a single hand-specimen (Figure 1c).

Where the cores of pillow lavas have been partly or completely epidotized, no structural or textural signs of contraction or expansion are visible in the surrounding spilitzed pillow rim. Figure 1a shows an example typical of hundreds of such cases observed in the field: the outlined pillow shows abundant outcrop-weathering fractures but no epidotized veinlets linking the epidosite nodule in the pillow core with the epidotized interpillow hyaloclastite. The absence of epidosite-age fractures shows that the spilitized pillow rim maintained its original volume intact during epidotization of the pillow core, consistent with the increase in porosity associated with the reaction (Harper, 1999). This key observation allows the spilite-to-epidosite reaction to be treated within a constant-volume framework, such that the bulk volume of minerals + pores in the spilite precursor equals the bulk volume of minerals + pores during progress of the reaction.

The lava-hosted epidosites investigated in the present study have an end-member mineralogy of epidote + quartz + titanite + hematite (Gilgen et al., 2016). They are mineralogically and chemically similar to the deep epidosites in the Samail SDC (Juteau et al., 2000; Nehlig et al., 1994; Rothery, 1983), but there are subtle differences. Magnetite is mainly present instead of hematite in the deep epidosites. Amphiboles (usually actinolite or hornblende) or chlorites are typical relict minerals in incompletely altered deep epidosites (Juteau et al., 2000; Nehlig et al., 1994; Rothery, 1983), whereas shallow epidosites commonly contain relict magmatic augite instead. Amphiboles are known to have replaced augite in the SDC during earlier spilite alteration, but they are relatively rare in spilitized lavas (Alabaster & Pearce, 1985; Smewing, 1975). Since the amphiboles pre-date epidotization (Nehlig et al., 1994), their presence or absence as relicts carries no implications for the temperature at which the epidosite alteration occurred. Fluid inclusion analyses in fact show that the Samail epidosites formed in the temperature range of 245–420°C, regardless of whether they are hosted by the SDC or the lavas (Richter & Diamond, 2019). That is, no systematic temperature gradient can be recognized between shallow and deep epidosites.
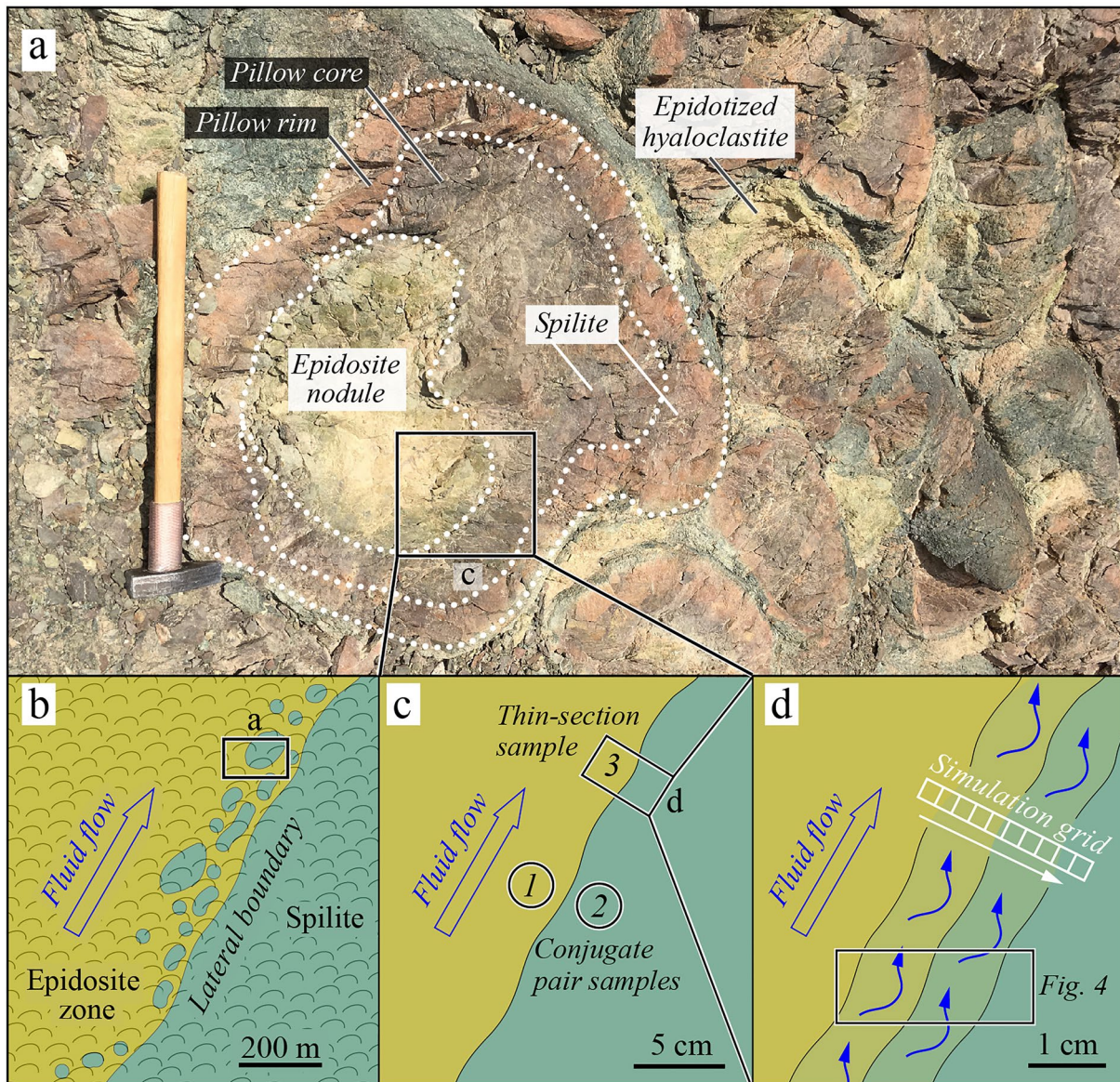
Figure 1. (a) Representative outcrop of patchy epidosite alteration in pillow lavas of the axial Geotimes unit, Rusays locality, Samail ophiolite. Top of pillow stack is to the right. Hammer is 60 cm long. Dotted outlines show an oblique section through a tubular pillow with a fine-grained rim and a coarser grained core, all surrounded by interpillow hyaloclastite. Reddish-brown color of pillow rim is due to oxidation of relict igneous titanomagnetite in shallow groundwater. Pale greenish-beige nodules of epidosite are present in pillow cores and interpillow hyaloclastite. These formed by fluid flow parallel to the long axes of the pillows (obliquely into or out of the plane of the photograph). The remainder of the outcrop is pervasively altered to spilite (note dark bluish-green chlorite rind around pillows). (b–d) Schematic vertical sections through altered pillow lavas at different spatial scales. (b) Large-scale features of an epidosite zone with patchy epidosite alteration along its lateral boundary. (c) Sampling positions of conjugate pairs of drill plugs (1 and 2) and of hand-specimens that traverse the reaction front, suitable for petrographic thin-sections (3). (d) Geometric relationship between reaction fronts, local flow directions (blue arrows), and orientation of numerical simulation grid (white arrow shows simulated flow direction).

3. Sampling

Samples were collected for this study along the north-eastern margin of the Samail ophiolite, mostly at epidosite zones described by Gilgen et al. (2016). Spilites and end-member epidosites, and samples with transitional mineralogy between these two, were taken from various depths in the SDC and the extrusive sequence. Locations of all samples are listed in Table S1 and details are given in Gilgen et al. (2016).

Ideally, we would have sampled profiles across the leading (downstream) boundaries of the epidosite zones. However, owing to the 20–50° dip of the ophiolite stratigraphy, such leading boundaries cannot be definitively identified in the field. We therefore sampled the lateral boundaries (Figure 1b) where sharp, dm-wide reaction fronts between spilite and epidosite are common (e.g., Figure 1a).

To enable quantification of the element transfers involved in epidosite alteration, sampling was aimed at obtaining rock pairs that represent reactant spilite and product epidosite in each of the main types of volcanic rock: pillowed flows, massive flows, and dikes. Samples were mostly extracted with a portable diamond-drill, yielding cylindrical, 2.5 cm diameter rock plugs up to 15 cm long. Preliminary analyses showed that the bulk composition of the spilites varies across individual outcrops in all these rock types. To avoid such variations, outcrops were sought where two rock plugs constituting a spilite-epidosite pair (Figure 1c) could be extracted in close proximity to each other (at ≤ 50 cm distance) within an individual pillow core, massive flow or dike. The plugs of each pair were later compared in the microscope to verify that they have matching ghost igneous textures. In total, 11 such conjugate pairs were collected, in each of which it is very likely that the spilite member closely represents the chemical and mineralogical precursor of the epidosite member. However, the intensity of epidosite alteration in the collected plugs is variable and few approach the end-member mineral assemblage.

Another aim of sampling was to collect rocks that record stages in the progressive alteration of spilite to epidosite. For this purpose, samples were taken of the cm-wide alteration haloes around epidosite nodules and epidote-quartz veins. These provide a complete reaction sequence from spilite to epidosite (e.g., Figures 1a and 1c). All such samples described in this manuscript were screened by thin-section microscopy to confirm that the alteration gradient is a product of variable epidosite alteration intensity only and not a product of inherited precursor rock heterogeneity. This was achieved by comparing the spilite texture to the ghost precursor texture in the epidosites (Section 5.2).

4. Analytical Methods

4.1. Scanning-Electron Microscope

Back-scattered electron (BSE) images were acquired using a Zeiss™ Evo50 scanning-electron microscope (SEM) with 20 kV beam acceleration and 2.5 mA current under low vacuum (28 Pa).

4.2. Mineral Chemistry

Mineral compositions were measured on a JEOL JXA-8200 electron-microprobe (EMPA) using a 15 kV, 10 nA focused beam. The elements Si, Ti, Al, Fe, Mn, Mg, Ca, Na, and K were measured on wavelength-dispersive spectrometers (WDS) and calibrated against natural albite (Na, Si) and orthoclase (K), and synthetic anorthite (Ca, Al), ilmenite (Ti), almandine (Fe), forsterite (Mg), and tephroite (Mn).

4.3. Mineral Maps

Maps of the minerals in petrographic thin-sections were acquired with the same EMPA instrument as above, with a 15 kV, 100 nA focused beam and acquisition times of 50 ms per spot. In addition to the nine elements measured by WDS (see above), Ni, Cr, F, Cl, Zr, S, and P were measured on an energy-dispersive spectrometer (EDS). Between 2.4 and 2.8 million spots were analyzed in each thin-section, following a square grid with 5 μm spacing. Mineral identification was carried out semi-automatically using XMapTools software (Lanari et al., 2019). This first entailed identifying the x-ray signal intensities of all minerals in the thin-section and then assigning each analyzed spot to the closest mineral composition.

4.4. Whole-Rock Elemental Analyses

All samples were powdered in an agate mill and weight loss on ignition (LOI) was measured by heating the powders for 2 h at 1050°C. Spilite samples AB16-4611, LD10-122-3, TB2-40b, and TB2-42c were mixed with 83 wt% dilithium tetraborate to produce homogeneous fused beads for analysis. Elemental compositions were measured on a PANalytical Axios™ WDS x-ray fluorescence (XRF) instrument at ETH-Zurich with

a rhodium source tube at voltages of 20–60 kV and currents of 40–100 mA according to the procedure described by Gilgen et al. (2014, 2016). Concentrations were calculated from a calibration curve established with 32 certified standards. Relative uncertainties of the major element concentrations were calculated from counting statistics, spectrometer drift and quality of the calibration curve, yielding <3% for Na and <1% for all other major elements. Replicate analyses of USGS standard basalts BCR-2 and BRP-1 during each analysis session yielded concentrations within error of their recommended compositions.

The spilite-epidosite pairs were analyzed by laser-ablation inductively coupled plasma spectrometry using the pressed-powder pellet (PPP-LA-ICP-MS) method of Peters and Pettke (2017). The analyses were conducted at the University of Bern with a GeoLas-Pro™ 193 nm ArF excimer laser coupled to an ELAN DRC-e™ quadrupole mass spectrometer. The principal calibration standard was the USGS basalt glass GSD-1G (reference values from Jochum et al., 2011). Measurement accuracy was checked by additional measurements of the highly depleted komatiite standard OKUM (Kane et al., 2007) and the basalt standard BRP-1 (Cotta & Enzweiler, 2008). Duplicate analyses of our samples by XRF yielded essentially identical results for the analyzed elements.

Any contamination by post-spilite and post-epidosite calcite was subtracted from the analyses by determining the total carbon content of aliquots of the sample powders in a Thermo Scientific FlashSmart™ carbon-nitrogen-sulfur (CNS) elemental analyzer, referenced to the LOI values.

4.5. Rock Density

The 22 2.5 cm diameter plugs that comprise the 11 conjugate sample pairs were dried, weighed and their bulk densities calculated from their dry mass and cylindrical dimensions. Values are listed in Table S1.

5. Petrographic and Geochemical Results

5.1. Spilite Reactants

The mineralogical and chemical compositions of spilites in the Samail ophiolite show a large variability, depending mainly on their original igneous composition and their temperature of alteration. Still, most spilites in the extrusive units can be assigned to one of two mineralogical groups. The first contains major amounts of albite (ab) and chlorite (chl), variable amounts of quartz (qtz) and epidote (ep), and minor hematite (hem), titanite (ttn) and sporadic actinolite, prehnite, and zeolites. Common accessories are Fe-Ti-oxides (magnetite, titanomagnetite, maghemite; Belgrano et al., 2019) and apatite, with rare pyrite and chalcopyrite. Late calcite, which formed after the spilite and epidosite alteration (Belgrano et al., 2019), is present as veinlets and as pore fillings in the immediately adjacent wall rocks. Volcanic textures are well preserved despite the pervasive hydrothermal alteration (Figures 2a and 2b). We refer to this reactant rock as "ab-chl spilite." The second group is characterized by the same mineralogy but with major amounts of relict igneous augite, here referred to as "ab-chl-aug spilite."

Figure 3 shows whole-rock analyses of 181 samples listed as spilites (gray dots) from all four volcanostratigraphic units in the Samail ophiolite (Belgrano et al., 2019). The mineralogy of all these samples was not checked exhaustively and they may contain additional alteration minerals (e.g., prehnite, zeolites) that are not part of the common spilite assemblage listed above. The large spread in compositions should therefore be viewed with care.

5.2. Epidosite Products

In thin-sections, end-member epidosites exhibit an idioblastic texture made up of intergrowths of equigranular, short prismatic, euhedral epidote and quartz crystals enclosing clouds of titanite inclusions and hematite flakes (Figures 2c and 2d). Titanite shows the same fine, equant crystal shapes as in the precursor spilite, whereas hematite is typically specular and coarser-grained than the earthy red variety in the spilites. Interstitial pores in the end-member epidosites are large (<500 μm in diameter) and have angular shapes imparted by the coarse crystal faces on their walls (Figures 2c and 2d). These textures are consistent with ep + qtz + hem + ttn coexisting as an equilibrium mineral assemblage.
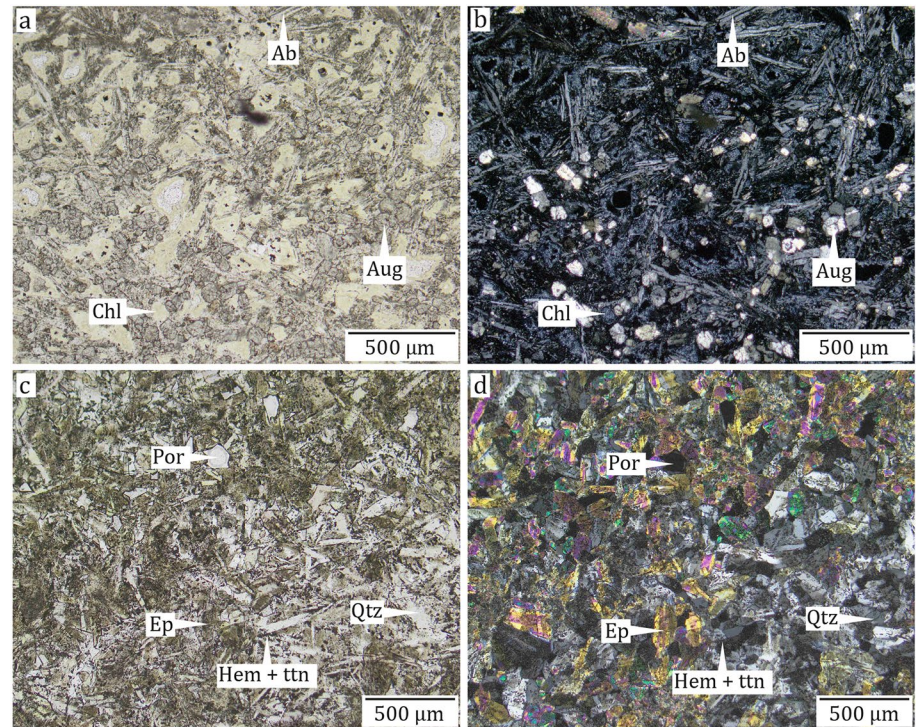
Figure 2. Textures of end-member spilites and epidosites in thin-section. (a) Plane-polarized and (b) cross-polarized, transmitted-light image of spilite (SG-113078) consisting of albite (ab), chlorite (chl), and augite (aug). (c) Plane-polarized and (d) cross-polarized, transmitted-light image of epidosite (LW5c), consisting mostly of epidote (ep) and quartz (qtz), with igneous "ghost" texture preserved by the distribution of fine hematite (hem) and titanite (ttn) crystals that outline the original plagioclase laths. Large interstitial pores (por) are characteristic for epidosites, indicating increase of porosity during epidosite alteration.

5.3. Reaction Fronts

Mineral maps of two petrographic sections across spilite-to-epidosite reaction fronts are shown in Figure 4. Figure 4a covers the transition from a partially epidotized ab-chl spilite in the distal zone (right) to a more advanced epidosite in the proximal zone (left), which still contains abundant relict chlorite. The mineral
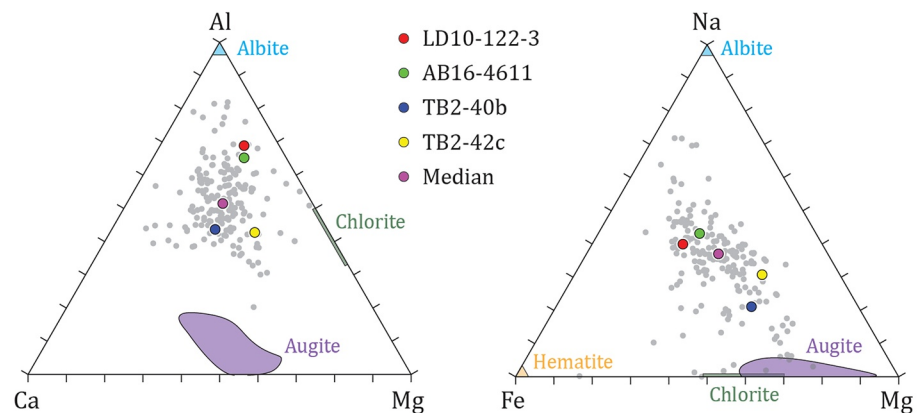
Figure 3. Spilite samples in Al-Ca-Mg and Na-Fe-Mg molar concentration plots. Gray dots are whole-rock compositions of 181 samples from all four volcanostratigraphic units in the Samail ophiolite (Belgrano et al., 2019). Colored dots mark four samples and the median composition of the entire data set. all selected for the numerical simulations. Colored fields show mineral compositions in the Samail spilites: augite from Belgrano et al. (2019); chlorite from Pflumio (1991).

Figure 4. Electron-microprobe mineral maps of two oblique cross-sections through spilite-to-epidosite reaction fronts, with spilite at right ("distal") and intermediate epidosite at left ("proximal"). 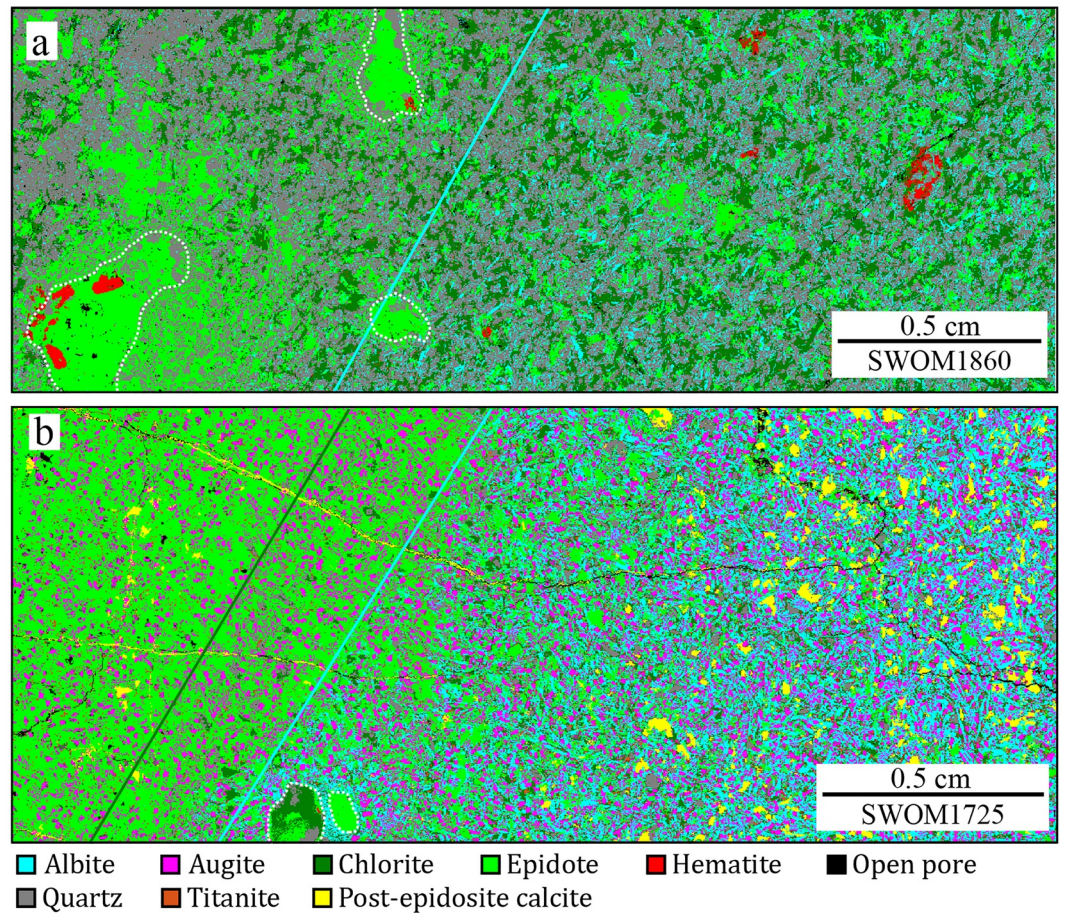See Figure 1 for field setting. Dotted white outlines denote former vesicles. Continuous lines parallel to the reaction fronts mark the approximate disappearance of reactant albite (light blue line) and chlorite (green line). Titanite in both images and hematite in the lower image are barely visible because of their very small crystal sizes (cf. Figures 2 and 5). Open pores are fractures and large interstitial cavities (see Figures 2 and 5 for more detail). Late calcite fills some epidosite-age pores in sample SWOM1725. (a) Augite-free, albite-chlorite spilite sample SWOM1860. (b) Albite-chlorite-augite spilite sample SWOM1725.

alteration sequence can be recognized despite the presence of large epidote-filled vesicles. Albite is progressively altered to epidote and quartz and is entirely replaced halfway across the map (blue lines in Figure 4). Chlorite is more stable and persists as a relict even in the most epidotized region of the map but is destroyed around the vesicles. Hematite abundance appears to decrease during the reaction whereas titanite appears to remain constant, though higher resolution maps would be required to verify this. The second mineral map (Figure 4b) shows the transition from an ab-chl-aug spilite (right) to an incomplete epidosite that still contains abundant relict augite (left). As in the ab-chl sample, albite is completely replaced in the distal zone (blue line), whereas chlorite survives to a more proximal position (green line). Augite remains abundant in the most altered region of the map. Again, hematite abundance appears to decrease during the reaction whereas titanite remains stable. The pore-filling calcite evident in Figure 4b post-dates epidosite alteration (as shown by cross-cutting relationships in dozens of thin sections) and it is therefore irrelevant to this study.

The high-magnification BSE images in Figure 5 show textures typical of the progress of the spilite-to-epidosite reaction in samples SWOM1725 and SWOM1851. The onset of alteration of the spilite is characterized by patchy replacement of albite laths by epidote and in some cases epidote + quartz (Figure 5a). This
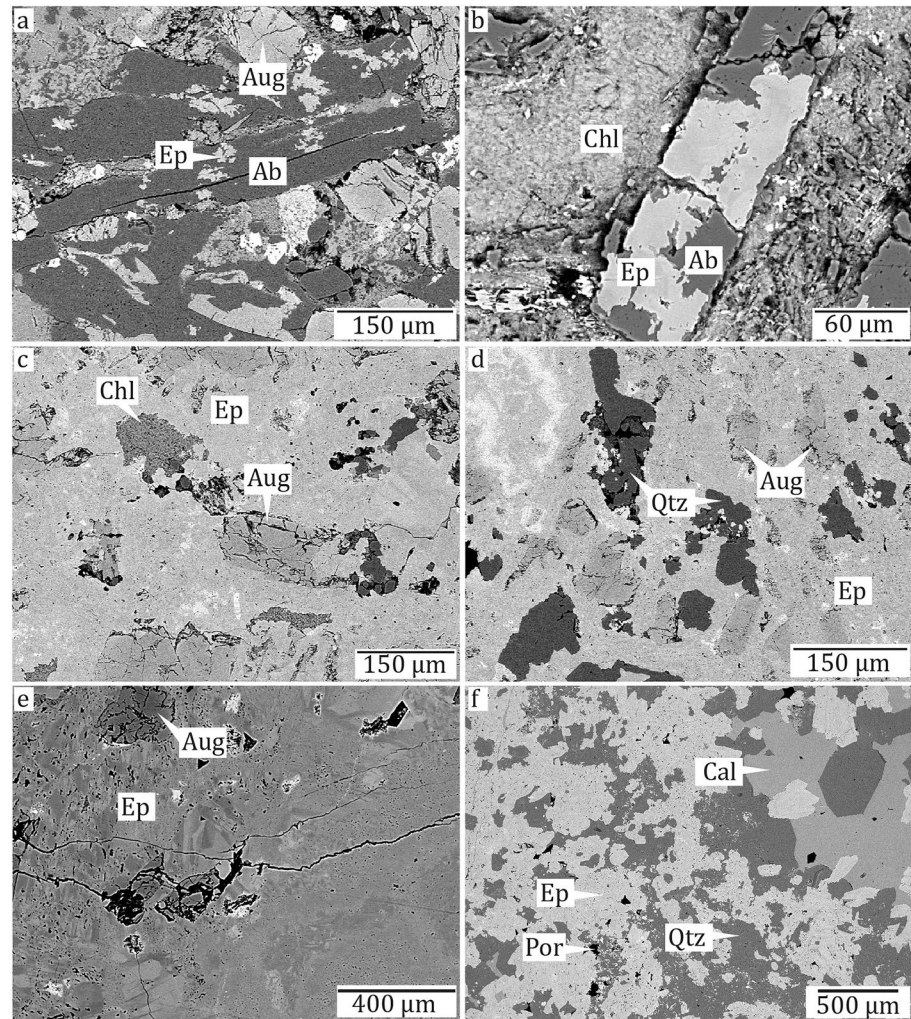
Figure 5. Backscattered-electron (BSE) images of samples SWOM1725 and SWOM1851 showing changes in mineral textures at different stages of epidosite alteration. Pores appear black. (a, b) Distal alteration near margin of spilite showing albite (ab) partially replaced by epidote (ep) whereas augite (aug) and chlorite (chl) are mostly unaltered. (c) Closer to the epidosite, chlorite is gradually replaced by epidote, but augite shows only weakly altered rims. (d) In the proximal alteration zone, augite is gradually dissolved while the matrix surrounding it is completely replaced by epidote and quartz (qtz). (e) Epidote exhibits BSE zonation due to significant Fe-Al compositional variation. (f) End-member epidosite exhibits equilibrium textures of euhedral epidote and quartz with large pores (por) in part filled by post-epidosite calcite.

stage is commonly accompanied by vesicle-filling epidote and quartz. More proximal alteration shows complete replacement of albite laths by epidote + quartz, whereas chlorite and augite are only slightly altered (Figure 5b). Closer to the epidosite, chlorite is gradually replaced by epidote, whereas augite is much more resistant to alteration (Figure 5c). In a more proximal position, alteration proceeds to the destruction of augite (Figure 5d). The reactant minerals albite and augite show no changes in their compositions due to the alteration, that is, they dissolve congruently. Chlorite also shows no distinct trends, although spot analyses are scattered (Figure S1 and Table S2). In contrast, individual epidote crystals frequently show strong Fe-Al zonation but its pattern appears to vary between adjacent crystals (Figure 5e; Table S3). The typical granoblastic texture and large interstitial pores of end-member epidosites are illustrated in Figure 5f, in which the coarse epidote and quartz crystals enclose much finer grains of titanite and hematite.
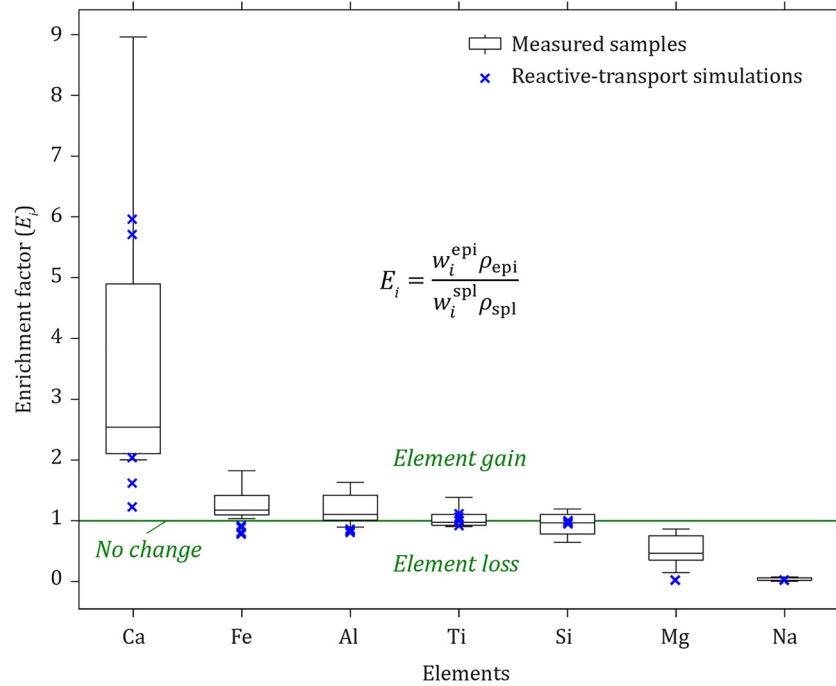
Figure 6. Analyzed versus simulated changes in element concentrations (mass or moles) caused by alteration of spilite to epidosite, normalized to constant total-rock volume. Values on *y*-axis show dimensionless enrichment relative to the spilite composition according to Equation 1: values > 1 indicate gain from the epidotizing fluid during epidosite alteration (e.g., value 3 indicates the threefold amount of an element, in mass or moles, relative to the precursor spilite); values < 1 indicate leaching and removal by the epidotizing fluid (e.g., value 0 indicates complete loss). Boxes and whiskers show elemental analyses (data in Table S4) of 11 conjugate spilite-epidosite rock pairs: middle horizontal line in each box represents median; bottom and top of each box represent first and third quartiles; whiskers mark minimum and maximum values. Blue crosses show predicted element changes for 5 spilite samples in Table 1, all of which have different starting compositions compared to the conjugate pairs. Predictions were made by reactive-transport simulations at 350°C, 50 MPa (see text), normalized according to Equation 1.

5.4. Mass Transfers During Spilite-to-Epidosite Alteration

The elemental compositions and densities of the 11 conjugate spilite-epidosite pairs, including three dike pairs from the SDC and eight pillow-core pairs from the axial Geotimes lava unit, are shown in Table S1. The sample set contains ab-chl, ab-chl-aug as well as ab-chl-act spilites. The latter are dikes from the SDC and they are included for completeness without detailed description. Their compositions do not differ systematically from the conjugate pairs sampled in the extrusive sequence.

The changes in element concentrations caused by the spilite-to-epidosite reaction were calculated from the data in Table S1 as follows:

$$E_i = \frac{w_i^{\mathrm{epi}} \rho_{\mathrm{epi}}}{w_i^{\mathrm{spl}} \rho_{\mathrm{spl}}} \tag{1}$$

where E is the dimensionless enrichment factor of the subscripted element i, w denotes the mass fraction of element i in the superscripted epidosite (epi) or spilite (spl), and ρ is the dry bulk mass-density of the subscripted rock. The numerical values of E are thus equivalent in mass and molar dimensions. The density normalization was made to obey the observed constraint of constant bulk-rock volume (minerals + pores) during the spilite-to-epidosite reaction (Section 2).

The resulting enrichment factors are plotted in Figure 6, where boxes and whiskers show the statistics for each element in the 11 conjugate pairs. Values of $E > 1$ indicate gain of the elements during the reaction. Values < 1 show removal during reaction, with the value 0 indicating complete loss. Thus, Na is almost
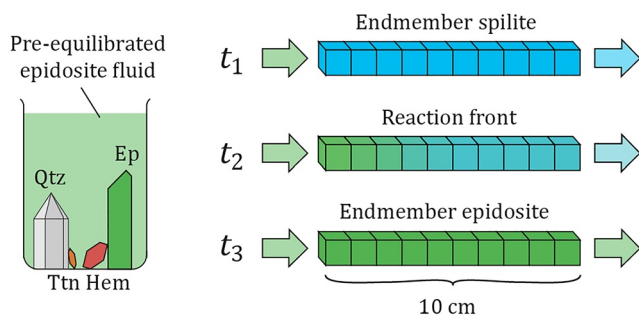
Figure 7. Setup of reactive-transport model (see orientation of grid in Figure 1d). Steps t_1–t_3 represent different times during the simulation.

completely leached from the samples, and Mg is consistently but only partially leached. In contrast, Ca shows huge additions to the rock and Fe also exhibits minor but consistent addition. Aluminum is mostly added, but this change is much less distinct than those of Ca, Mg, and Na. Titanium and silicon concentrations are conserved during epidosite alteration.

6. Reactive-Transport Modeling

6.1. Modeling Strategy

Although how and where the epidosite fluid is generated in the oceanic crust is not yet well defined, its chemical composition can be reconstructed by assuming equilibrium with the epidosite mineral assemblage and by drawing on solute concentrations from analyses of fluid inclusions in epidosites (see below). This approach does not presume a genetic link between epidosite fluids and seafloor vent fluids, in contrast to the calculations of Bettison-Varga et al. (1995), which used the composition of vent fluids to represent the epidosite fluid. By numerically simulating the passage of our reconstructed fluid through a model permeable spilite and enforcing the attainment of local equilibrium, the spilite is inevitably converted to epidosite. Monitoring the amount of fluid required for complete conversion yields the W/R ratio.

While the bulk volume of the model rock (minerals + pores) is held constant in the model, the volume fractions of minerals are allowed to change with reaction progress, in agreement with field observations: the spilite-to-epidosite transformation in our conjugate sample pairs is associated with a ∼10% decrease in the total mineral volume, which is consistent with the increase in porosity observed in other studies (e.g., Bettison-Varga et al., 1995; Cann et al., 2014; Harper et al., 1988). We limit our simulations to conditions during the formation of shallow epidosites in the Samail lavas, characterized by ep + qtz + hem + ttn equilibrium, and we omit the case of equilibrium with magnetite as observed in deep epidosites hosted by the SDC.

As noted in Section 3, our mineral maps and conjugate sample pairs derive from sharp reaction fronts that developed subparallel to the direction of advective fluid flow (blue arrows in Figure 1d), rather than perpendicular to flow. Nevertheless, we simulate the spilite-to-epidosite reaction using a model flow direction perpendicular to the true direction (white arrow in Figure 1d). This is based on the assumption that the mineralogical transformations across lateral boundaries match those across leading (downstream) boundaries of the large 100 m scale epidosite zones. Since we apply a local equilibrium model that is independent of time, the relative contributions of advective, diffusive, and dispersive solute transport have no influence on the model results.

6.2. Model Setup

Our numerical simulations were performed with the fully coupled reactive-transport code Flotran (Lichtner, 2007). Thermodynamic data were taken from version v.65.2018.09.25 of the Soltherm database (Reed & Palandri, 2006), which incorporates mineral properties from Holland and Powell (2011). All considered minerals and aqueous species are listed in Table S5. Flotran calculates the complete aqueous speciation and inventory of kinetically controlled fluid-mineral reactions at each pressure-temperature condition and time step. We have represented a simplified spilite-to-epidosite reaction zone as a 1D flow-through grid discretized into 10 cells (Figure 1d). The cells are initially assigned the mineralogical composition of a porous spilite precursor rock. As quantifying the rate of the epidosite-forming reaction is not a goal of this study, equilibrium is enforced by choosing a ratio of reaction rate to flow rate which essentially confines precipitating minerals to a saturation index (SI) < 1.001 and confines dissolving minerals to SI > 0.999. The simulations were performed at selected fixed temperatures between 250°C and 400°C, all at a pressure of 50 MPa, corresponding to representative conditions during the formation of epidosites in the Samail lavas (Richter & Diamond, 2019).

Figure 7 illustrates the model setup. At time t_1 the epidosite fluid commences flow through the model spilite from the left to the right. Since this injected fluid is in chemical disequilibrium with the spilite, it reacts and

undergoes compositional changes, dissolving some of the spilite minerals and replacing them with new epidosite minerals. A reaction front forms in the model (t_2) as the fluid equilibrates with each cell. Unreacted fluid continuously replaces the reacted fluid, such that the reaction front propagates along the array of cells. Once a portion of the rock is completely altered to end-member epidosite (t_3), the fluid no longer reacts with it, as fluid and rock are in mutual equilibrium. The mass of fluid required to form an epidosite equals the time-integrated mass of fluid that has passed through the model at the time at which a relict-free end-member epidosite mineralogy is achieved. Thus, the W/R ratio required to generate an end-member epidosite is calculated by dividing the required fluid mass by the mass of the initial spilite rock. Similarly, W/R ratios can be calculated for any intermediate step during the reaction toward the end-member epidosite assemblage.

6.3. Properties of Model Minerals

The thermodynamic properties of the model minerals were adapted to represent the measured compositions of the minerals across the reaction fronts (Section 5.3). For epidote, 27 intermediate members of an ideal solid-solution series were calculated from the thermodynamic properties of the epidote and clinozoisite end-members (Table S5). To test the highly variable compositions measured in natural chlorites (Tables S2 and S5), scoping simulations were performed with ideal Fe-Mg-chlorite solidsolutions but these produced unrealistically large compositional variations. The composition of chlorite was therefore fixed in the simulations as an intermediate member of an ideal daphnite-clinochlore solidsolution, which matches the average chlorite composition measured in the spilite samples (Figure 3, Table S2). In accord with the petrographic evidence for congruent dissolution of augite, its composition was also held constant in the simulations, using an intermediate member of an ideal diopside-hedenbergite solidsolution, which matches the average clinopyroxene composition in Geotimes lavas (Figure 3; Gilgen et al., 2014). Similarly, albite, which also undergoes congruent dissolution, was held constant at its pure composition. A member of an ideal albite-anorthite solidsolution was calculated to model the plagioclase in sample TB2-40b (Tables S5 and S6).

6.4. Composition of Reactant Spilites

We modeled the five samples indicated by colored dots in Figure 3 to explore the dependency of the W/R ratio on different mineralogical and chemical compositions of the reactant spilite. Among these samples are three that petrographically fall within the ab-chl and ab-chl-aug spilite groups and that cover the spread in the main cluster of bulk compositions. Their whole-rock elemental analyses (Table S1) were used to calculate their mineralogical compositions in terms of the common spilite minerals (Table 1), using pure hematite, titanite, and quartz, and the compositions of the other minerals specified in Section 6.3. The three samples include two ab-chl spilites (AB16-4611 and the very qtz-rich LD10-122-3) and one Mg-rich ab-chl-aug spilite (TB2-42c). Additionally, we chose a rather rare sample containing igneous plagioclase instead of albite (TB2-40b). Finally, we modeled an artificial sample ("Median") whose whole-rock elemental composition is the median of all 181 spilite samples in the database of Belgrano et al. (2019). The volume fractions of minerals were normalized to 95 vol%, leaving a nominal 5 vol% porosity that lies within the ~3–5 vol% range measured for Samail spilites (Christensen & Smewing, 1981). This value has no influence on the simulation results other than the normalization of the W/R ratios.

6.5. Composition of Epidosite Fluid

Three different sources of information were used to reconstruct the chemical composition of the epidosite fluid (Table 2 for a temperature of 350°C). First, we used the concentrations of Cl, Na, and Ca from analyses of primary fluid inclusions in epidosites (Richter & Diamond, 2019). The reported molalities for Cl (0.54) and Na (0.446) were used directly, and a value of 10 was taken from the range of reported values for the molal Na/Ca ratio.

Second, the absence of any mineral phases except for epidote, quartz, hematite and titanite in the end-member epidosites places limits on the possible values of pH and redox potential at the given Ca and Na concentrations. While each of the four epidosite minerals can occur at higher or lower pH, their combined and exclusive paragenesis delimits the stability of the epidosite fluid. To quantify these limits, hypothetical

Table 1

Mineralogical Compositions of the Five Selected Spilites in Figure 3, Simulated Compositions of Their Product Epidosites and Calculated Water/Rock (W/R) Mass Ratios Required to Convert the Spilites to End-Member Epidosites at Different Temperatures

Sample number[a] Rock type Volcanic unit	AB16-4611 Pillow flow Tholeiitic Alley	LD10-122-3 Pillow flow Lasail	TB2-40b Massive flow Geotimes	TB2-42c Pillow flow Boninitic Alley	Median[b] All units
Reactant spilite [c]					
Albite [vol%]	49.8	36.2	0	36.9	40.2
Plagioclase [vol%]	0	0	42.5	0	0
Augite [vol%]	1.2	0	26.4	23.6	13.8
Chlorite [vol%]	25.2	18.7	23.6	24.0	21.6
Epidote [vol%]	5.7	5.4	0	0	10.2
Hematite [vol%]	0.8	1.6	0.3	0	0.4
Quartz [vol%]	10.7	31.4	0	10.3	7.3
Titanite [vol%]	1.7	1.7	2.2	0.2	1.7
Nominal porosity [vol%]	5.0[c]	5.0[c]	5.0[c]	5.0[c]	5.0[c]
Product epidosites at 350°C [d]					
Quartz [vol%]	30.7	44.7	21.1	38.9	30.4
Epidote [vol%]	51.8	40.5	56.6	39.8	51.5
Hematite [vol%]	0	0	0	1.1	0.4
Titanite [vol%]	1.7	1.7	2.3	0.2	1.8
Porosity [vol%]	15.8	13.1	20.0	19.9	16.0
W/R ratio (250°C)	6,400	5,500	30,800	35,500	17,400
W/R ratio (300°C)	3,200	2,900	28,400	32,100	15,500
W/R ratio (350°C)	1,700	1,600	38,200	44,400	20,300
W/R ratio (400°C)	800	700	14,800	17,800	8,300

[a]Elemental analyses given in Table S1. [b]Median composition of all 181 spilites in database from Belgrano et al. (2019), as shown in Figure 3. [c]Mineral fractions in all spilite samples are forced to sum to 95 vol%, resulting in a nominal porosity of 5 vol%. [d]Simulated.

Table 2

Values of pH, Oxygen Fugacity and Total Element Concentrations of the Model Epidosite Fluid at 350°C and 50 MPa Compared to a Modern 350°C Vent Fluid at a Basaltic Mid-Ocean Ridge

Parameter	Modern vent fluid	Model concentration	Constrained by
pH	3.2 at 25 °C, 1 bar[a]	5.1	Epidosite stability field in Figure 8
log(fO_2)	−28 to −30.5[b]	−24	Conservation of 1×10^{-6} mol/kg H_2(aq) to stabilize hematite in absence of magnetite at 230–400 °C
Cl	5.58×10^{-1} mol/kg[a]	5.40×10^{-1} mol/kg	Fluid inclusion analyses in Richter and Diamond (2019)
Ca	3.4×10^{-2} mol/kg[a]	4.46×10^{-2} mol/kg	Fluid inclusion analyses in Richter and Diamond (2019)
Na	4.51×10^{-1} mol/kg[a]	4.46×10^{-1} mol/kg	Fluid inclusion analyses in Richter and Diamond (2019)
Si	1.21×10^{-2} mol/kg[a]	1.71×10^{-2} mol/kg	Quartz equilibrium
Al	–	9.10×10^{-7} mol/kg	Epidote equilibrium
Fe	1.25×10^{-2} mol/kg[a]	9.00×10^{-6} mol/kg	Hematite equilibrium
Ti	–	1.00×10^{-9} mol/kg	Titanite equilibrium
Mg	–	6.50×10^{-6} mol/kg	Value consistent with absence of an Mg-bearing mineral in the epidosite assemblage

[a]Brandon vent, orifice Bb.3, East Pacific Rise at 21° S (Van Damm et al., 2003). [b]Other basalt-hosted black smoker vents, East Pacific Rise at 11°–21° N (Kawasumi & Chiba, 2017).
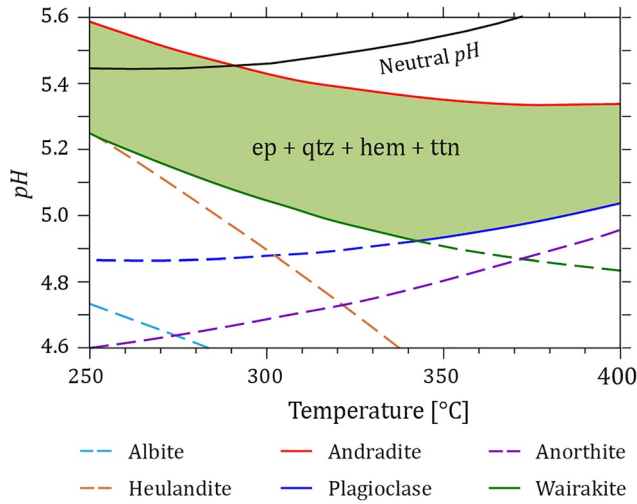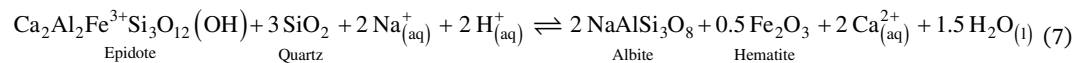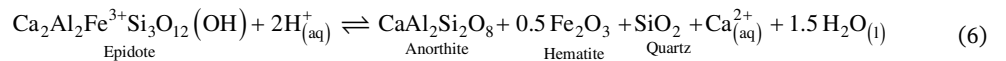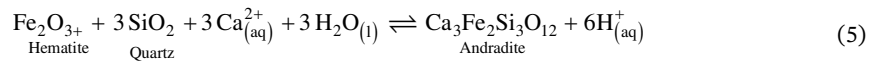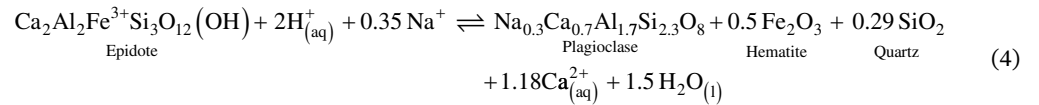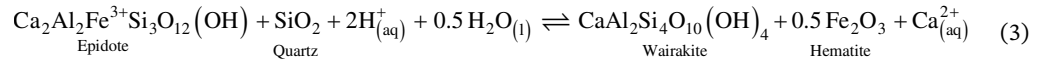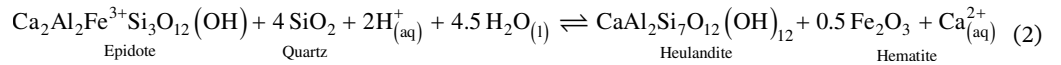
Figure 8. Temperature-pH stability of the epidosite mineral paragenesis (green field) involving epidote solid-solution + quartz + hematite + titanite at 50 MPa. Colored lines show equilibria between minerals in the legend and the epidosite assemblage according to Equations 2–7. Continuous curves denote stable equilibria and dashed curves denote metastable equilibria. Solid black line indicates neutral pH.

equilibria were calculated with numerous competitor minerals that fall within the compositional space of the epidosite assemblage (Table S5). The most stable of these equilibria are listed in Equations 2–7 (end-member epidote is shown for clarity but ideal solidsolutions were used in all calculations; excess titanite is stable with all the mineral assemblages and hence is not shown in Equations 2–7).

The pH constraints that reactions (2–7) imply are illustrated as a function of temperature in Figure 8. All curves in Figure 8 were calculated with Flotran using full chemical speciation including numerous aqueous chloride complexes (Table S5). At 250°C the hypothetical equilibrium involving ideal epidote solid-solution + quartz + hematite + titanite + heulandite limits the stability field of epidosite to a pH above 5.25 (reaction 2 and Figure 8). Just above 250°C, wairakite (reaction 3) becomes more stable with the epidosite assemblage than heulandite. Above 340°C, intermediate plagioclase (reaction 4) is more stable than wairakite and limits the epidosite stability field at low pH. On the high pH side, andradite is in equilibrium with quartz and hematite via reaction 5, and thus it delimits the epidosite stability field over the whole temperature range from 250°C to 400°C. Collectively, reactions 2–7 constrain the pH of the epidosite fluid tightly to within about 0.4 pH units between 4.90 and 5.34 at 350°C (Figure 8). We chose an intermediate pH of 5.1 for our simulations from 300°C to 400°C and 5.3 for the simulation at 250°C. Over the temperature and pH range in Figure 8, the molar Fe/(Fe + Al) ratio of the stable ideal epidote solid-solution was found to vary from 0.25 to 0.32 (not shown).

$$\underset{\text{Epidote}}{Ca_2Al_2Fe^{3+}Si_3O_{12}(OH)} + \underset{\text{Quartz}}{4\,SiO_2} + 2H^+_{(aq)} + 4.5\,H_2O_{(l)} \rightleftharpoons \underset{\text{Heulandite}}{CaAl_2Si_7O_{12}(OH)_{12}} + 0.5\,\underset{\text{Hematite}}{Fe_2O_3} + Ca^{2+}_{(aq)} \quad (2)$$

$$\underset{\text{Epidote}}{Ca_2Al_2Fe^{3+}Si_3O_{12}(OH)} + \underset{\text{Quartz}}{SiO_2} + 2H^+_{(aq)} + 0.5\,H_2O_{(l)} \rightleftharpoons \underset{\text{Wairakite}}{CaAl_2Si_4O_{10}(OH)_4} + 0.5\,\underset{\text{Hematite}}{Fe_2O_3} + Ca^{2+}_{(aq)} \quad (3)$$

$$\underset{\text{Epidote}}{Ca_2Al_2Fe^{3+}Si_3O_{12}(OH)} + 2H^+_{(aq)} + 0.35\,Na^+ \rightleftharpoons \underset{\text{Plagioclase}}{Na_{0.3}Ca_{0.7}Al_{1.7}Si_{2.3}O_8} + 0.5\,\underset{\text{Hematite}}{Fe_2O_3} + 0.29\,\underset{\text{Quartz}}{SiO_2}$$
$$+ 1.18\,Ca^{2+}_{(aq)} + 1.5\,H_2O_{(l)} \quad (4)$$

$$\underset{\text{Hematite}}{Fe_2O_{3+}} + 3\,\underset{\text{Quartz}}{SiO_2} + 3\,Ca^{2+}_{(aq)} + 3\,H_2O_{(l)} \rightleftharpoons \underset{\text{Andradite}}{Ca_3Fe_2Si_3O_{12}} + 6H^+_{(aq)} \quad (5)$$

$$\underset{\text{Epidote}}{Ca_2Al_2Fe^{3+}Si_3O_{12}(OH)} + 2H^+_{(aq)} \rightleftharpoons \underset{\text{Anorthite}}{CaAl_2Si_2O_8} + 0.5\,\underset{\text{Hematite}}{Fe_2O_3} + \underset{\text{Quartz}}{SiO_2} + Ca^{2+}_{(aq)} + 1.5\,H_2O_{(l)} \quad (6)$$

$$\underset{\text{Epidote}}{Ca_2Al_2Fe^{3+}Si_3O_{12}(OH)} + 3\,\underset{\text{Quartz}}{SiO_2} + 2\,Na^+_{(aq)} + 2\,H^+_{(aq)} \rightleftharpoons 2\,\underset{\text{Albite}}{NaAlSi_3O_8} + 0.5\,\underset{\text{Hematite}}{Fe_2O_3} + 2\,Ca^{2+}_{(aq)} + 1.5\,H_2O_{(l)} \quad (7)$$

Metastable equilibria are shown in Figure 8 by dashed lines. Both the anorthite + epidote + quartz + hematite + titanite assemblage (reaction 6) and the albite + epidote + quartz + hematite + titanite assemblage (reaction 7) are metastable over the entire temperature range. Intermediate plagioclase is more stable than the albite and anorthite end-members, such that albite-rich compositions are more stable at low temperatures and anorthite-rich compositions more stable at high temperatures. The composition of the most stable plagioclase changes across the temperature range. However, equilibrium between epidote + quartz + hematite + titanite and an ideal plagioclase with a fixed molar Ca/(Ca + Na) ratio of 0.7 is shown in Figure 7 for reference. This plagioclase is close to the measured composition of relict igneous plagioclase in our samples (Table S6) and it approximately matches the plagioclase inferred to be present in the deep rock buffer that controls the composition of certain seafloor vent fluids (Berndt & Seyfried, 1993).

The redox state of the epidosite fluid is not tightly constrained, but its lower limit can be calculated from the equilibrium of hematite and magnetite with the fictitious species O_2 (reaction 8).

$$\underset{\text{Hematite}}{3\,Fe_2O_3} \rightleftharpoons \underset{\text{Magnetite}}{2\,Fe_3O_4} + 0.5\,O_{2(aq)}$$

(8)

In reality, the species H_2O and H_2 would govern the redox state. For the simulations at 400 °C, $\log(fO_2)$ was set to -20, somewhat above value at the hematite-magnetite boundary. This value was chosen because it corresponds to 1×10^{-6} mol/kg H_2(aq), the maximum H_2 concentration that ensures the epidosite fluid remains in the hematite stability field at all temperatures between 400 and 230 °C. Simulations over this temperature range were therefore performed with the epidosite fluid at redox states defined by this H_2(aq) concentration.

Third, based on the fluid parameters and pressure-temperature conditions constrained above, the total aqueous Al, Si, Fe, and Ti concentrations in the fluid were calculated from equilibrium with the epidosite mineral assemblage. In the absence of an Mg-bearing phase in this assemblage, we are unable to calculate the concentration of Mg in the fluid directly. The fluid inclusion analyses of Richter and Diamond (2019) yield $1 \pm 0.5 \times 10^{-3}$ mol/kg for the Mg concentration at ~420°C, but values in this range are too high for our simulations at lower temperature. We therefore used the constraint that the Mg-concentration must be lower than the value at equilibrium with the epidosite assemblage plus augite, otherwise augite would not be dissolved during epidosite alteration. Accordingly, we set the Mg concentration to 1/4 of that achieved during the late stages of the model at 350°C, when the fluid is equilibrated with epidote + quartz + hematite + titanite + augite. This is a relatively low Mg concentration of 6.5×10^{-6} mol/kg.

6.6. Modeled Reaction Progress and Water/Rock Ratios

Figure 9 shows the simulated mineralogical evolution of the ab-chl sample LD10-122-3 and the ab-chl-aug Median sample during alteration to end-member epidosite at 350°C. The fluid composition in terms of major elements is shown in Figures 9c and 9d. The plotted curves represent values averaged over the whole model domain at each W/R ratio (in detail the values may vary between cells). This explains why the plotted aqueous element concentrations appear as smooth curves, rather than sharp steps. Non-averaged model results of the Median sample at selected W/R ratios are given in Figure S2 to illustrate this averaging over the system. The x-axis marks the cumulative W/R ratio increasing from left to right, showing that an increasing volume of fluid has passed through the model. This axis therefore correlates qualitatively with the temporal evolution during epidosite alteration.

In both simulations, albite is the first spilite mineral to be completely replaced by epidote and quartz. If augite is initially present (Figure 9b), it dissolves slowly, providing additional Ca required to form epidote from albite. Because the fluid cannot easily leach the excess Mg from the rock, a small amount of chlorite is formed. Thereafter, the residual augite is preserved until very high W/R ratios. In the absence of augite (Figure 9a), all the Ca to form new epidote must derive from the fluid. This explains why albite is destroyed at a higher W/R ratio of 250 in the augite-free sample compared to the augite-bearing sample (W/R ratio of 25). Thereafter, chlorite is altered to epidote, consuming some of the quartz produced by the destruction of albite. Augite is obviously extremely resistant to alteration. The Mg-concentration of the fluid in equilibrium with the rock drops off significantly after albite and chlorite are leached from the rock. This low, late-stage Mg-leaching capacity explains the high W/R ratios needed for complete epidosite alteration. Complete alteration of the ab-chl spilite is reached at a W/R ratio of 1,600, whereas the ab-chl-aug spilite requires a W/R ratio of 20,300. Titanite concentration remains constant in both cases and hematite is consumed during the reaction. However, hematite reappears during late-stage epidosite alteration of the ab-chl-aug spilite, when aug is being leached. In the ab-chl spilite the porosity increases from 5 to 13 vol%, whereas in the alb-chl-aug spilite the porosity increases from 5 to 16 vol% during alteration.

The product epidosite composition at 350°C and the calculated W/R ratios for all five selected samples at temperatures from 250 to 400°C are shown in Table 1. The W/R ratios required to completely alter these samples vary enormously, from 700 to 44,400. Values for ab-chl samples are generally much lower than those for ab-chl-aug samples. The W/R ratios for ab-chl samples decrease systematically with increasing temperature, whereas augite-bearing samples show a more complicated trend. In the latter case, W/R ratios decrease slightly from 250°C to 300°C. However, W/R ratios at these two temperatures cannot be directly compared because of the different pH used in the simulations. If the same pH were used at both temper-
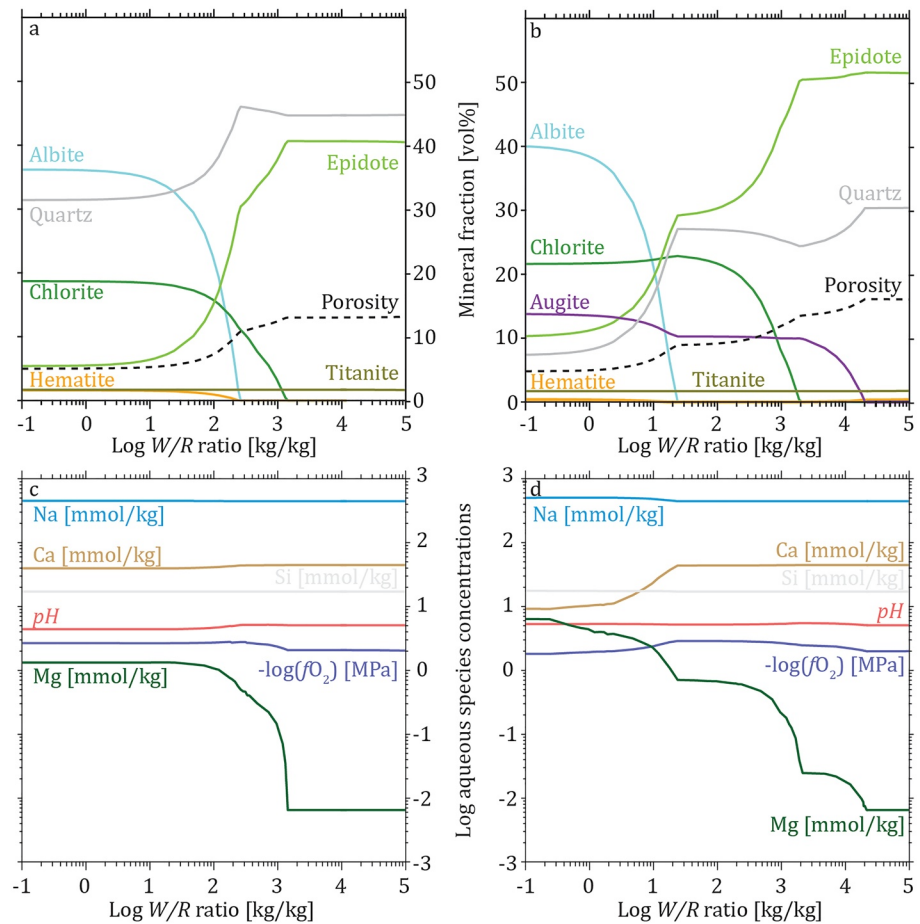
Figure 9. Simulated mineral evolution and selected total element concentrations, pH and oxygen fugacity of the fluid during increasing W/R ratio at 350°C and 50 MPa. Mineral fractions and element concentrations are averaged over the whole model domain. (a) Mineral fractions computed in sample LD10-122-3 (Table 1). (b) Mineral fractions computed in Median sample (Table 1). (c) Total aqueous element concentrations computed in sample LD10-122-3. (d) Total aqueous element concentrations computed in Median sample.

atures, the W/R ratios for ab-chl-aug spilites would increase from 250°C to 350°C. Above 350°C, the W/R ratios drop off significantly, with the values at 400°C being less than half those at 350°C. The spilite sample containing relict igneous plagioclase instead of albite (TB2-40b) does not behave significantly differently from the otherwise comparable sample containing albite (TB2-42c).

The relative gains and losses of elements calculated from the numerical simulations at 350°C of all five samples are listed in Table S4 and are indicated by blue crosses in Figure 6. Although the compositions of the reactant spilites used in the simulations are different from the plotted real samples, the predicted trends for Ca, Mg, and Na match the measured trends well. In the model, the end-member epidosites have by definition quantitatively lost all Mg and Na, whereas the natural epidosites are not end-members and so they contain significant amounts of relict Mg-bearing minerals. Iron and Al are partly removed from the rock in the simulations, whereas both have been enriched in the real rocks during epidosite alteration. The predicted conservation of Si and Ti fits the real samples nicely.

7. Discussion

7.1. Elemental Exchanges During the Spilite-To-Epidosite Reaction

The quantitative element exchanges plotted for the conjugate sample pairs in Figure 6 show extreme gains in Ca and losses in Na and Mg due to the spilite-to-epidosite reaction. The behavior of the other elements

(gains in Fe and Al, conservation of Ti and of Si) are more subtle and could in principle be affected by the assumptions underlying the diagram. The tight groupings of the minor element Ti and of the major element Si confirm that the analyzed sample sizes are sufficiently large to represent the compositions of the spilites and epidosites in outcrop.

The immobility of Ti in subseafloor hydrothermal systems is well established (e.g., Seyfried et al., 1988) but no assumptions regarding its mobility are inherent in Figure 6. Its conservation therefore independently confirms the constant bulk-rock volume constraint in Equation 1. For comparison, a 10% shrinkage of rock volume during epidosite alteration would balance median Al, but it would also shift the other elements to lower enrichment values as well, including immobile Ti, which is unrealistic. Shrinkage is also independently ruled out by the good match between the measured porosity change for the spilite-to-epidosite reaction and the porosity change calculated under the constraint of constant total-rock volume (Section 7.4). It follows that the observed enrichments in Fe and Al and conservation of Si cannot be ascribed to bulk-rock volume changes during alteration.

Previous studies also consistently report addition of Ca and leaching of Na and Mg in epidosites, even without correcting for sample density (Bettison-Varga et al., 1995; Nehlig et al., 1994; Richardson et al., 1987; Schiffman & Smith, 1988). However, trends for Si, Al, Fe are more diverse. Richardson et al. (1987) report systematic addition of Si in Troodos epidosites but unchanged Al and Fe concentrations. Schiffman and Smith (1988) found lower Al in Troodos epidosites relative to the host rocks but no systematic change in Si. Bettison-Varga et al. (1995) report that Al and Si in epidosites are not systematically different to the diabase rocks in the Troodos ophiolite. Nehlig et al. (1994) report that Si and Fe are leached and Al is added during epidosite alteration in the Samail SDC. The reasons for these differences in findings are unclear. Some spread may result from failure to sample conjugate spilite-epidosite pairs and some may be due to analytical uncertainties, but the spread may also reflect real variations in SDC-hosted epidosites.

7.2. Generality of the Reconstructed Spilite-To-Epidosite Reaction

The petrographic observations reported in Section 5 provide the basis to identify the direction and mechanism of the spilite-to-epidosite reaction at the dm-m scale, and to test the assumption of local equilibrium in our numerical simulations as a first approximation of the natural states driving the reaction.

The spatial replacement sequence from spilite toward end-member epidosite, involving the disappearance of albite followed by chlorite and then augite, is a characteristic feature of the numerous epidosite zones in the Samail ophiolite (listed in Gilgen et al., 2016), confirmed by thin-section petrography of more than a dozen reaction fronts. Across these fronts, the individual reactant crystals show increasingly corroded, non-crystallographic shapes and diminished crystals sizes, as expected for progressive hydrothermal dissolution. In contrast, the end-member epidosite product shows textures consistent with an equilibrium mineral assemblage: these include the intergrowths of smooth-faced, euhedral epidote, and quartz crystals, the increase in crystal sizes of hematite versus the spilite precursor, and the unchanging appearance of insoluble titanite despite complete replacement of all other spilite minerals. These observations thus define the direction and end-point of the spilite-to-epidosite reaction. Some studies report chlorite as part of the epidosite assemblage (e.g., Harper, 1995; Harper et al., 1988) but we view such rocks as intermediate members of the alteration series. Similarly, we consider the presence of actinolite needles in the deeper epidosites as relics of the more actinolite-rich spilite precursors.

Our analyzed samples derive from the lateral boundaries of the large epidosite zones (Figure 1b), because there we could readily find sharp fronts between end-member spilite and advanced intermediate or end-member epidosites (e.g., Figure 1a). However, deep within the large epidosite zones, for example throughout the km^2-size Ajeeb epidosite zone mapped by Gilgen et al. (2016), the mineralogy and textures of the intermediate and end-member epidosites are identical. We therefore conclude that our insights gained from the lateral boundaries are equally valid for the entire large-scale zones. Thus, huge volumes of epidotized rock can be explained by the same simple reaction mechanism. This simplicity suggests that fluid-rock interaction may have reached a steady state over significant periods at the km-scale. At any rate, it can be concluded that the observed variations in intensity of alteration deep within the epidosite zones

simply reflect variations in local *W/R* ratios determined by the heterogeneous and anisotropic permeability of the precursor spilitized lavas and sheeted dikes.

In addition to the control on alteration intensity by pre-existing permeability in the spilites, the increase in porosity due to the spilite-to-epidosite reaction also enhances permeability (e.g., Bettison-Varga et al., 1995; Cann et al., 2015; Harper et al., 1988). This provides a self-sustaining feedback to channel fluid into more intensely epidotized rocks, generating extremely steep alteration gradients between unaltered spilite and almost end-member epidosite over distances of just a few centimeter (e.g., Figure 1a). These alteration gradients translate to spatial gradients in *W/R* ratios of 10^2/cm to 10^3/cm.

7.3. Critical Features of the Model

Our model has several limitations. First of all, our quantitative results depend crucially on the thermodynamic properties used for the Mg minerals (clinochlore and diopside end-members within the chlorite and augite solid-solutions, respectively) and for the aqueous $MgCl^+$ complex, which accounts for almost all of the dissolved Mg. The properties for $MgCl^+$ in the Soltherm database are anchored at low temperature by the experiments of Majer and Štulík (1982) and constrained at high temperature by the experiments of Saccocia and Seyfried (1990), but the model fit is loose (Sverjensky et al., 1997). The measurements of Saccocia and Seyfried (1990) apply perfectly to the conditions in our simulations (300–400°C, 50 MPa). Using those values instead of the fitted properties would result in $MgCl^+$ concentrations about 20% higher than in our simulations, leading to *W/R* ratios that are 20% lower. To our knowledge, no newer studies are available to verify the Soltherm data. Regarding other potential Mg-bearing species such as carbonate complexes, we confirmed that high bicarbonate concentrations near calcite saturation do not influence the *W/R* ratios. To evaluate the $MgSO_4$ complex we used stability constants along the liquid-vapor curve of H_2O (Marshall, 1967) as a first approximation. Simulations with these data, extrapolated from temperatures ≤200°C, show that high sulfate concentrations close to anhydrite saturation would reduce the *W/R* ratios by only a few percent. If in nature another unknown Mg-complex is more stable than $MgCl^+$, then our presented *W/R* ratios would be too high. Increasing the Cl concentration in the epidosite fluid would decrease the *W/R* ratios, but the seawater chlorinity we used is well defined by fluid inclusion analyses (Richter & Diamond, 2019).

Second, in addition to the above dependencies there are uncertainties in the composition of the simulated input fluid. Although we know that the Mg concentration must be low enough to leach augite, the exact concentration is unknown. Choosing a higher Mg concentration in the input fluid closer to equilibrium with augite would result in *W/R* ratios much higher than presented here. The pH has a direct influence on the *W/R* ratios but it is well constrained to less than ±0.2 log units by reactions (2–7), thus its uncertainty has only a minor impact on calculated ratios. Moreover, all the minerals participating in the pH-constraining reactions have been observed in hydrothermal settings at temperatures and pressures comparable to conditions during epidosite alteration (Bird et al., 1984). We are therefore confident that these minerals would have formed during epidosite alteration if physicochemical conditions had been appropriate. The pH values we have derived (5.4 ± 0.2 at 250°C to 5.1 ± 0.2 at 350–400°C) are all close to neutral (i.e., at most 0.8 units below neutrality at 350–400°C; Figure 8). This finding contrasts with the suggestion by Seyfried et al. (1988) that the epidosite fluid should be more acidic, with pH around 3.5–4 at 350–400°C. Regarding the redox state, the only available constraint is that fluids forming epidosites in the Samail lavas are more oxidizing than the hematite-magnetite buffer, leaving a large uncertainty on the adopted value of −20 for log$f$(O_2) at 400°C. However, the redox state has no direct influence on the *W/R* ratio.

Third, we have simplified the epidosite-forming process in our model by assuming constant pressure, temperature, flux and fluid composition. In real systems, these conditions may change over time as indicated by the transient behavior of seafloor hydrothermal systems in response to igneous activity (e.g., Von Damm, 2000). Epidote zoning is common in real samples (Figure 5e and Cann et al., 2014), indicating that either temperature or fluid chemistry fluctuate during the alteration. This phenomenon is not treated explicitly in our model, but the influence of any given temperature fluctuation can be estimated from our simulations at different temperatures, since intermediate results must lie in-between the *W/R* ratios at different temperatures. On the other hand, any fluctuations in fluid chemistry during epidosite alteration

cannot be large, as the chemistry is relatively well constrained by the observations described above. Furthermore, the generality of the spilite-to-epidosite reaction throughout the Samail upper crust, as emphasized in Section 7.2, is broadly compatible with a large-scale steady state flow regime.

Fourthly, thermodynamic data predict that tremolite is more stable than augite over the whole 250–400°C temperature range, but neither tremolite nor actinolite is observed to form from augite during epidosite alteration. Where augite is present in the precursor spilite, it is congruently dissolved and concurrently replaced by the epidosite assemblage, without stabilizing amphibole as an intermediate phase. However, where actinolite is initially present in the precursor spilite instead of augite, the actinolite is dissolved as well rather than being altered to clinopyroxene, indicating that clinopyroxene is not more stable than actinolite. While tremolite appears to be thermodynamically more stable than augite, there must be a significant kinetic or energetic barrier that prevents replacement of augite by actinolite at epidosite-forming conditions. Berndt et al. (1989) reported from experiments at 350–425°C and 25–40 MPa that secondary amphiboles form from crushed basaltic glass but not from crushed holocrystalline basalt. This suggests that kinetics prevent actinolite from forming in crystalline rocks at these conditions. This agrees with independent evidence from the Samail ophiolite (Richter & Diamond, 2019), which show that actinolite needles require temperatures of 400–430°C and above to form during spilite alteration of crystalline rock (plagiogranite). The inferred kinetic inhibition was therefore taken into account in our simulations by suppressing the precipitation of amphiboles at $T \leq 400°C$.

Lastly, our simulations sometimes predict precipitation of wairakite, andradite, anorthite and a midrange plagioclase during intermediate stages of the reaction progress, but these minerals are not present in the natural samples displaying reaction fronts (e.g., Figure 4). This discrepancy indicates that the fluid composition evolves unrealistically during the simulations due to metastable assemblages, which implies that the local equilibrium model assumed in our simulations is not realistic in detail. For example, ab + chl + ep + qtz + hem + ttn is present in reality in early stages of the epidosite alteration, yet this assemblage is thermodynamically metastable with respect to our epidosite fluid over the whole temperature range (Figure 8). This assemblage would in principle buffer the fluid at a low pH, but lowering the fluid pH first induces precipitation of wairakite, heulandite, or anorthite. A likely reason why this does not occur in nature is that mineral kinetics are slow relative to fluid flow, and so equilibrium is not achieved during early stages of the alteration. Accordingly, Seyfried et al. (1988) assumed the fluid flow rate during epidotization to be high, such that the fluid determines the alteration mineralogy. In this case, the pH of the fluid would not be completely buffered by the rock and it would remain within the epidosite stability field during the entire alteration process. Simulations at suitably low Damköhler numbers to investigate this possibility were not carried out. Instead, the precipitation of the discrepant minerals was artificially suppressed in the simulations, to create the correct (observed) intermediate mineral assemblages.

7.4. Validation of the Model

Despite the above limitations, our model was able to reproduce many properties observed in real epidosites. Most importantly, we have reproduced end-member epidosites that consist of only epidote, quartz, hematite, and titanite. The predicted sequence of mineral alteration during epidotization fits that observed in our natural samples from the Samail upper crust (Figures 8 and 9) and also in the Troodos SDC (Cann et al., 2014). We have compared a modeled temporal evolution to the natural spatial variation in thin-sections (Figure 4), but the comparison is considered valid, as both phenomena are an expression of the same variable, namely a gradient in W/R ratio. Although samples were taken from lateral boundaries of the epidosite zones, the fluid composition was defined by parameters that are valid for end-member epidosites throughout the zones and their leading boundaries. The model results are therefore independent of where the reactions occur within the large km²-diameter Samail epidosite zones. The modeling results (Figure 9, Table 1) also show an increase in porosity from spilite-to-epidosite of about 10 vol.%, which matches laboratory measurements and qualitative deductions in other studies (e.g., Bettison-Varga et al., 1995; Harper et al., 1988).

In the Troodos SDC, Cann et al. (2014) reasoned from petrographic observations that epidotization proceeded by major dissolution of the precursor spilites, creating up to 20 vol.% porosity, after which epidosite minerals deposited in the void space, reducing the porosity to lower values. In contrast, in the lava- and

dike-hosted epidosites in the Samail ophiolite, ghost igneous textures of former glass and augite are well preserved by the arrangement of titanite and hematite inclusions, whereas areas without such inclusions (the feature that Cann et al., 2015 used to deduce major transient rock dissolution) are in our case interpreted to have been Fe- and Ti-free plagioclase crystals (or vesicles in the lavas). Moreover, the replacement textures across spilite-to-epidosite reaction fronts suggest gradual, coupled (i.e., simultaneous) dissolution-reprecipitation at the µm-scale at crystal interfaces (e.g., albite-epidote interface in Figure 5a). Our simulations predict a continuous increase in porosity with reaction progress (dashed curves in Figures 9a and 9b).

Our simulated element transfers during epidosite formation also closely replicate those of the real samples (Figure 6). The large gain of Ca by the rocks, the loss of Mg and Na and the conservation of Si and Ti are identical in the simulations and in nature. Regarding the conserved elements, a balanced enrichment factor for a conjugate pair comprising a spilite and an end-member epidosite would not necessarily imply element conservation during the whole reaction progress. However, the "epidosites" in our pairs represent a range of partially epidotized rocks, and therefore the indicated conservation of Si and Ti in Figure 6 suggests that these two elements were indeed conserved through at least much of the reaction progress. The real rocks show slight gains of Fe and Al, whereas the simulations predict net loss by leaching. This indicates that epidote and hematite were slightly supersaturated in the real input fluid, contrary to our equilibrium assumption. This is understandable if the input fluid was cooling during alteration. The observed lack of Si addition or removal throughout the reaction progress and the absence of any dissolution textures suggests that, remarkably, quartz was precisely saturated in the input fluid at the site of epidosite alteration. In this case, if the input fluid was indeed cooling, then it must have been slightly undersaturated with respect to quartz before entering the epidosite reaction zone, implying a quartz-free source rock for the fluid. Overall, the comparison between the simulations and the observations of the real rocks shows that the input fluid entirely determined not only the pH but also the chemical potentials of Na, Mg, and Ca in the epidosites. Therefore, these mobile major components (and other minor components with coherent behavior, such as Sr) can be viewed as having been externally buffered. In contrast, the spilite largely buffered the chemical potentials of the elements Fe, Al, Si, and Ti, such that additions or leaching by the fluid were minor (Fe, Al) or insignificant (Si, Ti).

7.5. Comparison With Water/Rock Ratios From Other Studies

Our calculated W/R ratios are much higher than previously published estimates, for various reasons. The W/R ratios based on Sr-isotopes (Kawahata et al., 2001) are around 20. The most likely reason for this low value is that it was calculated from a closed-system mass-balance with unmodified seawater. However, our deduced composition of the epidosite-forming fluid (Section 6.5) proves that it had been strongly modified by water-rock interaction before reaching equilibrium with the epidosite mineral assemblage. Therefore, prior to infiltrating a given volume of reactant spilite, each aliquot of epidosite fluid in nature already had a strontium isotope signature shifted toward the crustal value and thus its signature lay far from that of pristine seawater. Bickle and Teagle (1992) infer this deep downwelling flow to be pervasive with near equilibrium water-rock exchange, such that the Sr-isotopic ratio of the fluid is strongly shifted toward fresh volcanic rocks. It follows that the Kawahata et al. (2001) values are vast underestimates of true local W/R ratios for the epidosites; instead, they may better represent a bulk upper crustal ratio (see Section 7.7 below).

Water/rock ratios larger than 1,000 were estimated by Valsami and Cann (1992) from the addition of LREE during epidosite alteration. That study examined incomplete epidosites that contained significant amounts of relict chlorite and clinopyroxene. It follows that W/R ratios for end-member epidosites should be significantly higher.

The W/R ratios previously calculated by batch-reaction equilibrium models (Bettison-Varga et al., 1995) are as high as 1,250. Epidosites formed in these models always contain chlorite and are therefore not what we consider to be end-member epidosites. Their mineralogy is devoid of augite and is very similar to our sample LD10-122-3, for which our W/R ratio at 350°C (1,600) is comparable.

Seyfried et al. (1988) calculated the mass of fluid required to leach a significant portion of Mg from a precursor basalt by assuming an Mg-leaching capacity of 0.5 mmol/kg$_{H2O}$ (which is within the uncertainty of

the Mg concentration determined by Richter and Diamond (2019) in fluid inclusions from a Samail epidosite formed at 420°C). Thus, Seyfried et al. (1988) estimated a *W/R* ratio of around 1,000, but some of the chlorite remained in the epidosite. Our models show comparable Mg-concentrations during early stages of epidosite alteration. However, it is apparent from Figures 9c and 9d that the Mg-concentration in the fluid drops significantly after albite and chlorite are entirely destroyed. Magnesium is apparently not leached as efficiently as assumed by Seyfried et al. (1988) during late-stage epidosite alteration. Nevertheless, our *W/R* ratios calculated for augite-free assemblages at 400°C are comparable to the *W/R* ratio estimated by Seyfried et al. (1988).

Jowitt et al. (2012) studied interbanded epidosites and spilites in the Troodos SDC and came to very different conclusions compared to our study. They argued against the necessity of high *W/R* ratios to explain the epidosite mineralogy, and against buffering of this low-variance mineralogy by high fluxes of an external fluid. Emphasizing that chlorite- and amphibole-rich (spilite) rocks are spatially closely associated with the epidosites, Jowitt et al. (2012) reasoned from the similar Co/MgO ratios in these rocks that just one internally buffered fluid could have interacted with both alteration types, leaching Mg from the epidosites and redepositing it locally (at the dm-scale) to synchronously enrich the adjacent chlorite- and amphibolite-rich spilites. Jowitt et al. (2012) stated that this mechanism invalidates the high *W/R* ratios in the literature and explains the similar Sr-isotope ratios of the two alteration types. In view of the low solubility of Mg (Sections 6.5, 7.3) we presume this implies that the same fluid was recycled multiple times between epidosite and spilite, enriching the spilites in Mg at the same time as the epidosites were being generated. Contrary to the model of Jowitt et al. (2012), there is clear evidence in the Samail ophiolite (Section 7.2) that the chlorite and amphibole in the spilites pre-date the epidosites, and very large volumes of epidosite exist with no spatially associated spilites anomalously enriched in Mg. Moreover, we cannot envisage any gradients in chemical potential at the dm-m scale that would allow multiple cycles of Mg dissolution and reprecipitation by the same aliquot of fluid. Finally, the assumption that *W/R* ratios based on Sr-isotopes reflect local conditions is discussed further below.

7.6. Comparison of Model Epidosite Fluid With Modern Seafloor Vent Fluid

Earlier studies have proposed that epidosite-forming fluids ascend to create massive sulfide deposits at black smoker vents on the basaltic seafloor (e.g., Cann et al., 2014; Jowitt et al., 2012; Richardson et al., 1987; Schiffman & Smith, 1988). On the other hand, owing to the lack of epidosites in drill cores from MOR crust distant from convergent plate boundaries, other researchers have suggested that epidosites occur only in suprasubduction-zone settings, as represented by the Troodos and Samail ophiolites (Gillis & Banerjee, 2000). We have not needed to presume a link to black smoker fluids in order to perform our study; therefore it is interesting to compare the composition of our model epidosite fluid with that of modern vent fluids.

At the outset, it can be noted that black smoker type vent fluids produce quartz + pyrite + Fe-chlorite ± sericite alteration in subseafloor stockworks at fluid-dominated conditions, which significantly differs from epidosite alteration. This dissimilarity hints that at least some fluid parameters must differ between the two fluids.

Modern vent fluids span a wide range of chemical compositions determined by numerous factors including their temperature, fluid pathway, amount of subsurface mixing, host lithology and extent of phase separation (e.g., Von Damm, 2000; Von Damm & Bischoff, 1987; Von Damm et al., 1985, 2003). The Brandon vent (orifice Bb.3) at the East Pacific Rise was chosen for comparison with our model epidosite fluid (Table 2) because of its similar basaltic host rocks, temperature close to 350°C and salinity close to seawater (Von Damm et al., 2003). The concentrations of Na are nearly equal in both fluids. Concentrations of Ca differ somewhat, but are comparable inasmuch as Ca is strongly enriched relative to seawater. The Si content of the vent fluid is significantly lower than in our model fluid. This can be explained by the drop in silica solubility during ascent to the lower pressure of the seafloor, and shallow subseafloor mixing with recharging seawater may reinforce this effect. The pH in the Brandon vent fluid (and many other MOR vent fluids worldwide) is very low (3.2 at 25 °C) compared to our model pH (~5.1 ± 0.2). The pH of black smoker vent fluids is strongly influenced by the precipitation of sulfides from dissolved Fe^{2+} and H_2S at and below the seafloor, which strongly acidifies the spent fluid. Sulfides are ubiquitous in high-temperature black smoker vents but are absent from the epidosites examined in this study. A pH significantly higher than that observed in modern vent

fluids was measured in various experiments where basalt, basalt glass or spilite was reacted with modified seawater (e.g., Berndt et al., 1989; Seyfried & Bischoff, 1981). Berndt et al. (1989) point out that their pH values represent minimum constraints on the in situ fluids because sulfides may have precipitated prior to their pH measurements during the quenching step necessitated by their experimental method. The lack of sulfide precipitation in epidosites might therefore account for the near-neutral pH of the model epidosite fluid.

Another significant difference with respect to vent fluids is that our model fluid is notably more oxidized. Sulfide typically dominates over sulfate in vent fluids, indicating strongly reducing conditions, whereas if we add sulfur to our model fluid, sulfate complexes dominate over sulfide complexes. A possible explanation for such a difference in redox potential is that the source rocks for epidosite fluids contain a lower abundance of reducing agents than the source rocks for typical black-smoker fluids. This could indicate that sulfides, as a prominent reducing agent, had been leached from the source rocks and possibly transported to the seafloor to generate sulfide mineral deposits before ongoing fluid-rock interaction generated the epidosite fluid. This suggests that long-lived fluid circulation may be required to create epidosite fluids and hence cause epidosite alteration upon fluid ascent. This fits the late, post-spreading-axis timing of epidosite alteration in the Samail ophiolite, which led to overprinting of the footwalls and hanging-walls of axial massive sulfide deposits (Gilgen et al., 2016).

The most striking difference visible in Table 2 is the 10^4 higher concentration of Fe in the vent fluid versus our model epidosite fluid. Given the comparable chlorinities and assuming the same sulfur contents, the solubility of Fe in the two fluids is mostly controlled by pH and oxidation state. If the pH of the vent fluid is indeed lowered by near-seafloor precipitation of sulfide minerals, then it is much higher Fe concentration can be attributed to its lower oxidation potential. Regardless of the true sulfur content of the epidosite fluid, the extremely low Fe concentration is a serious obstacle to the proposal (e.g., Cann et al., 2014; Jowitt et al., 2012; Richardson et al., 1987; Schiffman & Smith, 1988) that the epidosite fluid is the deep equivalent of black smoker vent fluids and hence that the epidosite fluid could form massive pyrite deposits once it has ascended to the seafloor. It seems more likely that epidosite fluids discharge without forming significant accumulations of sulfide minerals, although precipitation of anhydrite is likely upon mixing with seawater.

7.7. Implications

The W/R ratios required to form end-member epidosites are extremely high but they place only minimum bounds on the amount of fluid that passed through the rock in nature. This is because once the equilibrium mineral assemblage is attained, further passage of fluid leaves no mineralogical trace in the rock. However, such end-member rocks constitute only a small fraction of the Samail epidosite zones. Where augite or actinolite are present in the precursor spilites, these reactant minerals are usually preserved in the epidosites (as in our spilite-epidosite pairs). This indicates that the high W/R ratios implicated in quantitatively leaching augite are rarely achieved. As soon as all albite is destroyed, the rock visually appears strongly epidotized in the field, even though the W/R ratio at that stage is only a small fraction of the ratio needed for complete alteration. This hinders the determination of alteration intensity in the field. The average W/R ratio of the large epidosite zones such as those mapped by Gilgen et al. (2016) is therefore likely much lower than the W/R ratio presented here for end-member epidosite alteration. Indeed, very few of the rocks termed epidosite in the literature contain less than the 1 wt% MgO commensurate with complet. alteration, but almost all of them are virtually Na-free (Bettison-Varga et al., 1995; Harper, 1995; Harper et al., 1988; Jowitt et al., 2012; Nehlig et al., 1994; Reed & Morgan, 1971; Schiffman & Smith, 1988; Valsami & Cann, 1992; Wang et al., 2012). Nonetheless, the large volumes of intermediate epidosites mapped in the Samail and Troodos ophiolites (e.g., Gilgen et al., 2016; Richardson et al., 1987: Schiffman & Smith, 1988) still require enormous volumes of fluid to have circulated through them.

If we assume that the average epidosite in the km³-size zones in the Samail and Troodos ophiolites are intermediate reaction products, meaning that all their albite and half their original chlorite have been destroyed, then the amount of fluid required to create these zones can be calculated. The corresponding intermediate point for the Median sample in Figure 9 yields an average W/R ratio of 700 at 350°C and 50 MPa. This ratio means that 700 kg of epidosite-equilibrated fluid are required to convert just 1 kg of spilite to an intermediate epidosite. It follows that to create 1 km³ (2.82×10^{12} kg) of intermediate epidosite, 1.97×10^{15} kg of
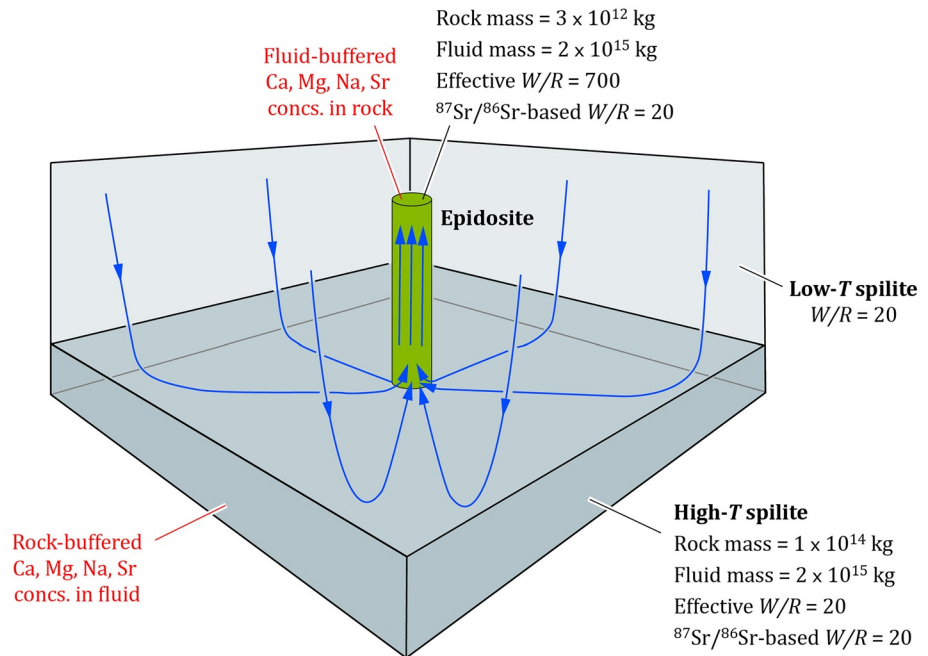
Figure 10. Schematic 3-D block of oceanic crust showing pervasive downflow of seawater through low-T spilites into a deep high-T alteration zone (dark gray), where the fluid attains a rock-buffered chemical and Sr-isotope composition (effective W/R ratio ∼20). Near-seafloor region is not shown. Focusing and ascent of the rock-buffered fluid (stream lines) through a relatively narrow (0.5–1 km wide) upflow zone leads to fluid decompression and cooling, altering the precursor low-T spilite to epidosite (green). The ascending fluid reaches effective W/R ratios ∼700, imposing its chemical potentials of Na, Mg, Ca, Sr, and Sr-isotopes onto the epidosite, resulting in Sr-isotope-based W/R ratios ∼20.

epidosite fluid are required. Clearly, epidosites deserve to be viewed as field markers of the passage of vast amounts of hydrothermal fluid.

Although we cannot directly investigate the genesis of the epidosite fluids with our simulations, the fluids are likely to have acquired their composition via interactions of basaltic rocks with high-T spilite fluid at relatively low W/R ratios, such that the fluid chemistry remains rock-buffered (particularly with respect to Na, Mg, Ca, and Sr). Assuming these reaction-zone rocks experience a W/R ratio comparable to typical spilites (∼20), ∼1×10^{14} kg of rock buffer are required for each 1 km^3 of intermediate epidosite, corresponding to 35 times the mass of epidosite. All the fluid in this large mass of high-T rock must be focused into a relatively narrow, fluid-dominated upflow zone to produce epidosite from precursor spilite (Figure 10). In addition to this hydraulic focusing, a mechanism is required to bring the high-T rock-buffered fluid into equilibrium with the epidosite mineral assemblage. We speculate that cooling and/or decompression could induce this change, but this proposal needs testing by further simulations.

How can our huge solubility-based W/R ratios for the epidosites be reconciled with those of other W/R monitors? For example, ratios derived for epidosites from Sr isotopes are typically very low (e.g., ∼20; Section 7.5) because epidosites have similar $_{87}$Sr/^{86}Sr ratios to spilites (Bickle & Teagle, 1992). We have argued that our solubility-based W/R ratios represent true (effective) local values. In contrast, we suggest that the W/R ratios based on Sr-isotopes are inherited from processes along the entire downflow path of seawater through the oceanic crust. This includes the high-T segment where the epidosite fluid attains a rock-buffered Sr concentration and Sr-isotope signature, as described above (Figure 10), in accordance with Bickle and Teagle (1992). Focusing of overwhelming amounts of this fluid into the upflow zone imposes the inherited Sr-isotope composition onto the epidosite, resulting in calculated W/R ratios of ∼20. Thus, when viewed within the context of crustal-scale fluid circulation, the small W/R ratios calculated from Sr-isotopes in epidosites are not in conflict with the huge local W/R ratios implied by the spilite-to-epidosite reaction.

8. Conclusions

Our results support previous studies that have identified epidosites as paleo-upflow zones of hydrothermal fluids through the magmatically heated oceanic crust. Field relations in the Samail ophiolite have shown that epidosite alteration occurs systematically later than spilite alteration and that it overprints early massive sulfide deposits. New petrographic and geochemical observations have revealed the reaction mechanism by which epidosite alters the Samail lavas and SDC. Epidosite replaces basalts that had already been pervasively spilitized by high temperature water-rock interaction. No evidence was found for direct replacement of fresh basalt lavas or dikes to epidosite. The spatial sequence of alteration from end-member spilite to epidosite occurs across reaction zones only cm-dm wide. Moving toward the epidosite, albite is the first spilite mineral replaced by epidosite and quartz, followed by chlorite and finally relict igneous augite (if present in the initial spilite), resulting in an end-member epidosite assemblage of equigranular epidote + quartz + titanite + hematite (or magnetite in SDC samples). Calcium is strongly enriched in the epidosites, with minor enrichment of Fe and Al. Silicon and Ti are conserved throughout the reaction sequence, and Mg and Na are quantitatively removed. This simple reaction mechanism accounts for the mineralogy and textures of epidosites throughout the large km^2-scale epidosite zones exposed in the Samail upper crust.

Combining thermodynamic calculations with published elemental analyses of primary fluid inclusions in end-member epidosites allows the chemical composition of the epidosite fluid to be reconstructed. The pH of the epidosite fluid is tightly constrained to 5.4 ± 0.2 at 250°C and 5.1 ± 0.2 at 350–400°C (≤0.8 units below neutrality). For epidosites in the lava sequence, the redox state is constrained by hematite stability, implying low $H_2(aq)$ content (~ 1×10^{-6} mol/kg). Owing to this high oxidation state and near-neutral pH, Fe concentration in the epidosite fluid is also low (4×10^{-6} at 250 °C and 6×10^{-5} mol/kg at 400 °C) and any dissolved sulfur is dominantly present as sulfate species. By contrast, typical black smoker vent fluids are much more reducing and acidic, they contain 200–3000 times more Fe (10^{-2} mol/kg) and are rich in dissolved sulfide. These chemical characteristics appear incompatible with the proposal that epidosite fluids are deep equivalents of black-smoker type fluids. It is likely that epidosite fluids would precipitate anhydrite upon venting but improbable that they could form a large pyrite deposit. Given the late timing of epidosite alteration, we suggest that epidosite fluids post-date the ascent of black-smoker type fluids, possibly within the same upflow zones.

Numerical reactive-transport simulations of the spilite-to-epidosite reaction at 50 MPa and 250–400°C yield the minimum W/R ratios required to form end-member epidosites. The values depend mainly on the mineralogical composition of the precursor spilite rock and on the temperature of reaction. For example, augite-free ab + chl spilites require W/R mass ratios (kg_{fluid}/kg_{rock}) of 5,500 at 250°C or 700 at 400°C. In spilites rich in highly insoluble augite (e.g., ~25 vol.%), minimum W/R ratios at the same temperatures vary from 35,500 to 17,800. These numbers rely heavily on the thermodynamic properties used in the model, particularly those for Mg complexes, but uncertainties are probably less than 20%. The W/R ratios derived from end-member epidosites are minimum estimates, as once the rock has reached equilibrium with the input fluid it cannot undergo further alteration and hence it cannot record further fluid throughput.

Recognizing that the chemical potentials of Na, Mg, Ca, and Sr in epidosites are buffered by the influxing external fluid allows the meaning of different W/R monitors to be interpreted. Our solubility-based W/R ratios strictly represent local values: for instance, $W/R = 700$ implies 700 kg of fluid passed through each kg of epidosite in outcrop. In contrast, classical W/R ratios calculated from Sr-isotopes reflect the cumulative water-rock interaction along the downflow path of seawater through to its equilibration with high temperature spilitized rock deep in the crust. The epidosite fluid transports this rock-buffered Sr-isotope composition into the upflow zone and imposes it, without significant modification, on the epidosite. Therefore, the low W/R ratios calculated from such isotope signatures do not record how much fluid has passed through an outcrop of epidosite.

End-member epidosites are relatively rare in the Samail occurrences, and intermediate reaction products containing residual chlorite or augite make up most of the epidosite zones. The W/R ratios of intermediate epidosites (700–1,000) are therefore more relevant for assessing large-scale fluid flow. These ratios are nominally exact, as they have not exhausted their capacity to record reaction progress. Thus, epidosites are sensitive flow meters that record a range of four orders of magnitude in the amount of fluid that has passed through the rock. The W/R ratios imply that 2×10^{15} kg of epidosite fluid are required to form each km^3 of intermediate epi-

dosite. This confirms the view that epidosites are witnesses of vast amounts of upwelling hydrothermal fluid. The fluid properties and *W/R* ratios that we have derived will serve as useful calibration targets for hydraulic-thermal-chemical simulations of upflow zones. The results also provide stringent constraints for future studies of how and where the epidosite fluid is generated, and how its pathways to the seafloor can be tracked.

Data Availability Statement

All data necessary to support our research are publicly available at the zenodo repository (https://doi.org/10.5281/zenodo.4723993).

References

Alabaster, T., & Pearce, J. A. (1985). The interrelationship between magmatic and ore-forming hydrothermal processes in the Oman ophiolite. *Economic Geology*, *80*, 1–16. https://doi.org/10.2113/gsecongeo.80.1.1

Alt, J. C. (1995). Subseafloor processes in mid-ocean ridge hydrothennal systems. *Geophysical Monograph*, *91*, 85–114. https://doi.org/10.1029/GM091p0085

Banerjee, N. R., Gillis, K. M., & Muehlenbachs, K. (2000). Discovery of epidosites in a modern oceanic setting, the Tonga forearc. *Geology*, *28*, 151–154. https://doi.org/10.1130/0091-7613(2000)28%3C151:DOEIAM%3E2.0.CO;2

Belgrano, T. M., & Diamond, L. W. (2019). Subduction-zone contributions to axial volcanism in the Oman-U.A.E. ophiolite. *Lithosphere*, *11*(3), 399–411. https://doi.org/10.1130/L1045.1

Belgrano, T. M., Diamond, L. W., Vogt, Y., Biedermann, A. R., & Gilgen, S. A. (2019). A revised map of volcanic units in the Oman ophiolite: Insights into the architecture of an oceanic proto-arc volcanic sequence. *Solid Earth*, *10*, 1181–1217. https://doi.org/10.5194/se-10-1181-2019

Berndt, M. E., & Seyfried, W. E. (1993). Calcium and sodium exchange during hydrothermal alteration of calcic plagioclase at 400°C and 400 bars. *Geochimica et Cosmochimica Acta*, *57*, 4445–4451. https://doi.org/10.1016/0016-7037(93)90494-H

Berndt, M. E., Seyfried, W. E., & Janecky, D. R. (1989). Plagioclase and epidote buffering of cation ratios in mid-ocean ridge hydrothermal fluids: Experimental results in and near the supercritical region. *Geochimica et Cosmochimica Acta*, *53*, 2283–2300. https://doi.org/10.1016/0016-7037(89)90351-7

Bettison-Varga, L., Schiffman, P., & Janecky, D. R. (1995). Fluid-rock interaction in the hydrothermal upflow zone of the Solea graben, Troodos ophiolite, Cyprus. *Geological Society of America Special Paper*, *296*, 81–100. https://doi.org/10.1130/SPE296-p81

Bickle, M. J., & Teagle, D. A. H. (1992). Strontium alteration in the Troodos ophiolite: Implications for fluid fluxes and geochemical transport in mid-ocean ridge hydrothermal systems. *Earth and Planetary Science Letters*, *113*, 219–237. https://doi.org/10.1016/0012-821x(92)90221-g

Bird, D. K., Schiffman, P., Elders, W. A., Williams, A. E., & McDowell, D. S. (1984). Calc-silicate mineralization in active geothermal systems. *Economic Geology*, *79*, 671–695. https://doi.org/10.2113/gsecongeo.79.4.671

Cann, J. R. (1969). Spilites from the Carlsberg Ridge, Indian Ocean. *Journal of Petrology*, *10*, 1–19. https://doi.org/10.1093/petrology/10.1.1

Cann, J. R., Mccaig, A. M., & Yardley, B. W. D. (2014). Rapid generation of reaction permeability in the roots of black smoker systems, Troodos ophiolite, Cyprus. *Geofluids*, *15*, 179–192. https://doi.org/10.1111/gfl.12117

Cann, J. R., Mccaig, A. M., & Yardley, B. W. D. (2015). Rapid generation of reaction permeability in the roots of black smoker systems, Troodos ophiolite, Cyprus. *Geofluids*, *15*, 179–192. https://doi.org/10.1111/gfl.12117

Christensen, N. I., & Smewing, J. D. (1981). Geology and seismic structure of the northern section of the Oman ophiolite. *Journal of Geophysical Research*, *86*, 2545–2555. https://doi.org/10.1029/JB086iB04p02545

Cotta, A. J. B., & Enzweiler, J. (2008). Certificate of analysis of the reference material BRP-1 (Basalt Ribeirão Preto). *Geostandards and Geoanalytical Research*, *32*, 231–235. https://doi.org/10.1111/j.1751-908X.2008.00894.x

Galley, A. G. (1993). Characteristics of semi-conformable alteration zones associated with volcanogenic massive sulfide districts. *Journal of Geochemical Exploration*, *48*(2), 175–200. https://doi.org/10.1016/0375-6742(93)90004-6

Gilgen, S. A., Diamond, L. W., & Mercolli, I. (2016). Sub-seafloor epidosite alteration: Timing, depth and stratigraphic distribution in the Semail ophiolite, Oman. *Lithos*, *260*, 191–210. https://doi.org/10.1016/j.lithos.2016.05.014

Gilgen, S. A., Diamond, L. W., Mercolli, I., Al-Tobi, K., Maidment, D. W., Close, R., & Al-Towaya, A. (2014). Volcanostratigraphic controls on the occurrence of massive sulfide deposits in the Semail Ophiolite, Oman. *Economic Geology*, *109*, 1585–1610. https://doi.org/10.2113/econgeo.109.6.1585

Gillis, K., & Banerjee, N. R. (2000). Hydrothermal alteration patterns in supra-subduction zone ophiolites. *Special Papers - Geological Society of America*, 283–297. https://doi.org/10.1130/0-8137-2349-3.283

Hannington, M. D., Santaguida, F., Kjarsgaard, I. M., & Cathles, L. M. (2002). Regional-scale hydrothermal alteration in the Central Blake River Group, western Abitibi subprovince, Canada: Implications for VMS prospectivity. *Mineralium Deposita*, *38*(4), 393–422. https://doi.org/10.1007/s00126-002-0298-z

Harper, G. D. (1995). Pumpellyosite and prehnitite associated with epidosite in the Josephine ophiolite - Ca metasomatism during upwelling of hydrothermal fluids at a spreading axis. *Geological Society of America Special Paper*, *296*, 101–122. https://doi.org/10.1130/spe296-p101

Harper, G. D. (1999). Structural styles of hydrothermal discharge in ophiolite/sea-floor systems. In C. T. Barrie, & M. D. Hannington (Eds.), Volcanic-associated massive sulfide deposits: Processes and examples in modern and ancient settings. Reviews in Economic Geology (Vol. 8, pp. 53–73).

Harper, G. D., Bowman, J. R., & Kuhns, R. (1988). A field, chemical, and stable isotope study of subseafloor metamorphism of the Josephine Ophiolite, California-Oregon. *Journal of Geophysical Research*, *93*, 4625–4656. https://doi.org/10.1029/jb093ib05p04625

Holland, T. J. B., & Powell, R. (2011). An improved and extended internally consistent thermodynamic dataset for phases of petrological interest, involving a new equation of state for solids. *Journal of Metamorphic Geology*, *29*, 333–383. https://doi.org/10.1111/j.1525-1314.2010.00923.x

Humphris, S. E., & Klein, F. (2018). Progress in Deciphering the Controls on the Geochemistry of Fluids in Seafloor Hydrothermal Systems. *Annual Review of Marine Science*, *10*, 315–343. https://doi.org/10.1146/annurev-marine-121916-063233

Jochum, K. P., Wilson, S. A., Abouchami, W., Amini, M., Chmeleff, J., Eisenhauer, A., et al. (2011). GSD-1G and MPI-DING reference glasses for in situ and bulk isotopic determination. *Geostandards and Geoanalytical Research*, *35*, 193–226. https://doi.org/10.1111/j.1751-908X.2010.00114.x

Jowitt, S. M., Jenkin, G. R. T., Coogan, L. A., & Naden, J. (2012). Quantifying the release of base metals from source rocks for volcanogenic massive sulfide deposits: Effects of protolith composition and alteration mineralogy. *Journal of Geochemical Exploration*, *118*, 47–59. https://doi.org/10.1016/j.gexplo.2012.04.005

Juteau, T., Manac'h, G., Moreau, O., Lécuyer, C., & Ramboz, C. (2000). The high temperature reaction zone of the Oman ophiolite: New field data, microthermometry of fluid inclusions, PIXE analyses and oxygen isotopic ratios. *Marine Geophysical Researches*, *21*, 351–385. https://doi.org/10.1023/a:1026798811446

Kane, J. S., Potts, P. J., Meisel, T., & Wiedenbeck, M. (2007). International Association of Geoanalysts' protocol for the certification of geological and environmental reference materials: A supplement. *Geostandards and Geoanalytical Research*, *31*(3), 285–288. https://doi.org/10.1111/j.1751-908X.2007.00869.x

Kawahata, H., Nohara, M., Ishizuka, H., Hasebe, S., & Chiba, H. (2001). Sr isotope geochemistry and hydrothermal alteration of the Oman ophiolite. *Journal of Geophysical Research*, *106*, 11083–11099. https://doi.org/10.1029/2000jb900456

Kawasumi, S., & Chiba, H. (2017). Redox state of seafloor hydrothermal fluids and its effect on sulfide mineralization. *Chemical Geology*, *451*, 25–37. https://doi.org/10.1016/j.chemgeo.2017.01.001

Lanari, P., Vho, A., Bovay, T., Airaghi, L., & Centrella, S. (2019). Quantitative compositional mapping of mineral phases by electron probe micro-analyzer. *Geological Society, London, Special Publications*, *478*(1), 39–63. https://doi.org/10.1144/sp478.4

Lichtner, P. C. (2007). *FLOTRAN user's manual: Two-phase nonisothermal coupled thermal-hydrologic-chemical (THC) reactive flow & transport code, version 2*. Los Alamos National Laboratory.

Lippard, S. J., Shelton, A. W., & Gass, I. G. (1986). *The ophiolite of northern Oman*. (p. 165). Blackwell Scientific Publications Ltd.

Majer, V., & Štulík, K. (1982). A study of the stability of alkaline-earth metal complexes with fluoride and chloride ions at various temperatures by potentiometry with ion-selective electrodes. *Talanta*, *29*, 145–148. https://doi.org/10.1016/0039-9140(82)80039-8

Marshall, W. L. (1967). Aqueous systems at high temperature. XX. Dissociation constant and thermodynamic functions for magnesium sulfate to 200°C. *Journal of Physical Chemistry*, *71*, 3584–3588. https://doi.org/10.1021/j100870a036

Mottl, M. J. (1983). Hydrothermal processes at seafloor spreading centers: Application of basalt-seawater experimental results. In P. A. Rona, K. Boström, L. Laubier, & K. L. Smith (Eds.), Hydrothermal processes at seafloor spreading centers. NATO Conference Series (IV marine sciences) (Vol. 12). Springer.

Nehlig, P., Juteau, T., Bendel, V., & Cotten, J. (1994). The root zones of oceanic hydrothermal systems: Constraints from the Samail ophiolite (Oman). *Journal of Geophysical Research*, *99*, 4703–4713. https://doi.org/10.1029/93jb02663

Peters, D., & Pettke, T. (2017). Evaluation of major to ultra trace element bulk rock chemical analysis of nanoparticulate pressed powder pellets by LA-ICP-MS. *Geostandards and Geoanalytical Research*, *41*(1), 5–28. https://doi.org/10.1111/ggr.12125

Pflumio, C. (1991). Evidences for polyphased oceanic alteration of the extrusive sequence of the Semail ophiolite from the Salahi Block (Northern Oman). In *Ophiolite genesis and evolution of the oceanic lithosphere* (pp. 313–351). Springer. https://doi.org/10.1007/978-94-011-3358-6_17

Polat, A., Appel, P. W. U., Frei, R., Pan, Y., Dilek, Y., Ordóñez-Calderón, J. C., et al. (2007). Field and geochemical characteristics of the Mesoarchean (~3075 Ma) Ivisaartoq greenstone belt, southern West Greenland: Evidence for seafloor hydrothermal alteration in supra-subduction oceanic crust. *Gondwana Research*, *11*, 69–91. https://doi.org/10.1016/j.gr.2006.02.004

Quon, S. H., & Ehlers, E. G. (1963). Rocks of northern part of Mid-Atlantic Ridge. *The Geological Society of America Bulletin*, *74*, 1–8. https://doi.org/10.1130/0016-7606(1963)74[1:ronpom]2.0.co;2

Reed, J. C., & Morgan, B. A. (1971). Chemical alteration and spilitization of the Catoctin Greenstones, Shenandoah National Park, Virginia. *Geology*, *79*, 526–548. https://doi.org/10.1086/627674

Reed, M., & Palandri, J. (2006). *SOLTHERM. H06, a database of equilibrium constants for minerals and aqueous species*. University of Oregon.

Richardson, C. J., Cann, J. R., Richards, H. G., & Cowan, J. G. (1987). Metal-depleted root zones of the Troodos ore-forming hydrothermal systems, Cyprus. *Earth and Planetary Science Letters*, *84*, 243–253. https://doi.org/10.1016/0012-821x(87)90089-6

Richter, L., & Diamond, L. W. (2019). Identifying deep hydrothermal fluids that leach metals from the oceanic crust and generate seafloor VMS deposits. In Proceedings of 15th Biennial SGA Meeting, Glasgow, Scotland. Society for Geology Applied to Mineral Deposits (SGA) (Vol. 1, pp. 76–79).

Rothery, D. A. (1983). The base of a sheeted dyke complex, Oman ophiolite :implications for magma chambers at oceanic spreading axes. *Journal of the Geological Society of London*, *140*, 287–296. https://doi.org/10.1144/gsjgs.140.2.0287

Saccocia, P. J., & Seyfried, W. E. (1990). Talc-quartz equilibria and the stability of magnesium chloride complexes in NaCl-MgCl$_2$ solutions at 300, 350, and 400°C, 500 bars. *Geochimica et Cosmochimica Acta*, *54*, 3283–3294. https://doi.org/10.1016/0016-7037(90)90285-s

Schiffman, P., & Smith, B. M. (1988). Petrology and oxygen isotope geochemistry of a fossil seawater hydrothermal system within the Solea Graben, northern Troodos ophiolite, Cyprus. *Journal of Geophysical Research*, *93*, 4612–4624. https://doi.org/10.1029/jb093ib05p04612

Seyfried, W. E., Berndt, M. E., & Seewald, J. S. (1988). Hydrothermal alteration processes at mid-ocean ridges: Constraints from diabase alteration experiments, hot-spring fluids and composition of the oceanic crust. *The Canadian Mineralogist*, *26*, 787–804.

Seyfried, W. E., & Bischoff, J. L. (1981). Experimental seawater-basalt interaction at 300 C, 500 bars, chemical exchange, secondary mineral formation and implications for the transport of heavy metals. *Geochimica et Cosmochimica Acta*, *45*(2), 135–147. https://doi.org/10.1016/0016-7037(81)90157-5

Smewing, J. D. (1975). *Metamorphism of the Troodos massif, Cyprus*. (Ph.D. Thesis). Open University.

Staudigel, H. (2003). Hydrothermal alteration processes in the oceanic crust. In R. L. Rudnick (Ed.), Treatise on geochemistry (Vol. 3, pp. 511–535). https://doi.org/10.1016/b0-08-043751-6/03032-2

Sverjensky, D. A., Shock, E. L., & Helgeson, H. C. (1997). Prediction of the thermodynamic properties of aqueous metal complexes to 1000°C and 5 kb. *Geochimica et Cosmochimica Acta*, *61*, 1359–1412. https://doi.org/10.1016/s0016-7037(97)00009-4

Valsami, E. & Cann, J. R. (1992). Mobility of rare earth elements in zones of intense hydrothermal alteration in the Pindos ophiolite, Greece. *Geological Society - Special Publications*, *60*, 219–232. https://doi.org/10.1144/gsl.sp.1992.060.01.13

Varga, R. J., Gee, J. S., Bettison-Varga, L., Anderson, R. S., & Johnson, C. L. (1999). Early establishment of seafloor hydrothermal systems during structural extension: Paleomagnetic evidence from the Troodos ophiolite, Cyprus. *Earth and Planetary Science Letters*, *171*(2), 221–235. https://doi.org/10.1016/S0012-821X(99)00147-8

Von Damm, K. L. (2000). Chemistry of hydrothermal vent fluids from 9°-10°N , East Pacific Rise: "Time zero," the immediate posteruptive period. *Journal of Geophysical Research*, *105*, 11203–11222. https://doi.org/10.1029/1999jb900414

Von Damm, K. L., & Bischoff, J. L. (1987). Chemistry of hydrothermal solutions from the southern Juan de Fuca Ridge. *Journal of Geophysical Research: Solid Earth*, *92*(B11), 11334–11346. https://doi.org/10.1029/JB092iB11p11334

Von Damm, K. L., Edmond, J. M., Grant, B., Measures, C. I., Walden, B., & Weiss, R. F. (1985). Chemistry of submarine hydrothermal solutions at 21° N, East Pacific Rise. *Geochimica et Cosmochimica Acta*, *49*(11), 2197–2220. https://doi.org/10.1016/0016-7037(85)90222-4

Von Damm, K. L., Lilley, M. D., Shanks, W. C., Iii, Brockington, M., Bray, A. M., O'grady, K. M., et al. (2003). Extraordinary phase separation and segregation in vent fluids from the southern East Pacific Rise. *Earth and Planetary Science Letters*, *206*(3–4), 365–378. https://doi.org/10.1016/S0012-821X(02)01081-6

Wang, J., Kusky, T. M., Polat, A., Wang, L., Peng, S., Jiang, X., et al. (2012). Sea-floor metamorphism recorded in epidosites from the ca. 1.0 Ga Miaowan ophiolite, Huangling anticline, China. *Journal of Earth Sciences*, *23*, 696–704. https://doi.org/10.1007/s12583-012-0288-8

White, A. J. R., Smith, R. E., Nadoll, P., & Legras, M. (2014). Regional-scale Metasomatism in the Fortescue Group Volcanics, Hamersley Basin, Western Australia: Implications for hydrothermal ore systems. *Journal of Petrology*, *55*(5), 977–1009. https://doi.org/10.1093/petrology/egu013

References From the Supporting Information

Butterfield, D. A., Massoth, G. J., McDuff, R. E., Lupton, J. E., & Lilley, M. D. (1990). Geochemistry of hydrothermal fluids from Axial Seamount hydrothermal emissions study vent field, Juan de Fuca Ridge: Subseafloor boiling and subsequent fluid‐rock interaction. *Journal of Geophysical Research*, *95*(B8), 12895–12921. https://doi.org/10.1029/JB095iB08p12895

James, R. H., Green, D. R., Stock, M. J., Alker, B. J., Banerjee, N. R., Cole, C., et al. (2014). Composition of hydrothermal fluids and mineralogy of associated chimney material on the East Scotia Ridge back-arc spreading centre. *Geochimica et Cosmochimica Acta*, *139*, 47–71. https://doi.org/10.1016/j.gca.2014.04.024

Levitus, S., Burgett, R., & Boyer, T. P. (1994). World Ocean Atlas 1994 (Vol. 3). Salinity (No. PB-95-270104/XAB; NESDIS-3). National Environmental Satellite, Data, and Information Service.

Millero, F. J., Feistel, R., Wright, D. G., & McDougall, T. J. (2008). The composition of Standard Seawater and the definition of the reference-composition salinity scale. *Deep Sea Research Part I: Oceanographic Research Papers*, *55*(1), 50–72. https://doi.org/10.1016/j.dsr.2007.10.001

Pettke, T., Oberli, F., Audétat, A., Guillong, M., Simon, A. C., Hanley, J. J., & Klemm, L. M. (2012). Recent developments in element concentration and isotope ratio analysis of individual fluid inclusions by laser ablation single and multiple collector ICP-MS. *Ore Geology Reviews*, *44*, 10-38. https://doi.org/10.1016/j.oregeorev.2011.11.001

Seyfried, W. E., & Ding, K. (1995). Phase equilibria in subseafloor hydrothermal systems: A review of the role of redox, temperature, pH and dissolved Cl on the chemistry of hot spring fluids at mid‐ocean ridges. *Seafloor Hydrothermal Systems: Physical, Chemical, Biological, and Geological Interactions*, *91*, 248-272. https://doi.org/10.1029/GM091p0248

Weber, S. & Diamond, L. W. (2019) Epidosite alteration of oceanic crust: quantifying water–rock ratios with reactive-transport modeling. In *Proceedings of the 15th Biennial SGA Meeting*.

Erratum

The originally-published version of this article presented modeling results based on a fixed, nominal redox state ($\log(fO_2) = -20$ bar) consistent with hematite stability. This incidentally implied unjustifiably low Fe concentrations in the epidosite fluid over the lower part of the modeled temperature range. During the review process, a comparison of the modeled epidosite fluid to modern black-smoker fluids was added; unlike the modeling results, this comparison is very sensitive to redox state. The corrected version of this article adopts a fixed amount of dissolved hydrogen as the control on redox state in the progressively cooling epidosite fluid. Corrections have been made to the Abstract, Table 2, and the body of the article, notably the first paragraph of page 15 and the second paragraph of page 24. The qualitative conclusions of the article are unchanged. This may be considered the official version of record.